An Eulerian Scheme for Identifying Fronts and Vortices in Quasi-Balanced Flows

SCOTT D. BACHMAN[a]

[a] *Climate and Global Dynamics Laboratory, National Center for Atmospheric Research, Boulder, Colorado*

(Manuscript received 15 February 2021, in final form 2 August 2021)

ABSTRACT: The identification of vortices in a fluid flow is a dynamically interesting problem that has practical applications in oceanography due to the outsized role eddies play in water mass, heat, and tracer transport. Here a new Eulerian scheme is developed to detect both vortices and strongly strained fronts, which are both ubiquitous in the World Ocean. The new scheme is conceptually linked to the well-known Okubo–Weiss parameter, but is extended to quasigeostrophic flows by recognizing the strong role played by vertical shear in ocean dynamics. Adapted from the λ_2 criterion for vortex identification, the scheme considers the curvature of the pressure field as the differentiator between vortical and strained flow structures, and it is shown that its underlying geometry also exhibits characteristics of quasigeostrophic flow. The uses and skill of the scheme are demonstrated using a high-resolution regional ocean simulation, and prospects for its use with observational products are discussed.

KEYWORDS: Eddies; Fronts; Large-scale motions

1. Introduction

The stratification and small aspect ratio of ocean mesoscale flows often makes them well approximated by two-dimensional (2D) dynamics. Even with the vast simplifications afforded by approximating mesoscale motions in this way, the emergent flow structures often bear excellent qualitative and dynamical resemblance to real ocean turbulence. Two-dimensional flows feature analogous cascades of enstrophy and energy as do quasigeostrophic (QG) flows, and in the presence of a Coriolis force bear similar flow structures such as vortices, jets, and filaments (Herring 1980; McWilliams 1984; Hua and Haidvogel 1986; McWilliams 1989). The generation of filaments has been of particular interest in the context of both two- and three-dimensional flows (e.g., Ashurst et al. 1987; Melander et al. 1987; Dritschel et al. 1991; Ohkitani and Kishiba 1995; Galanti et al. 1997; Kevlahan and Farge 1997; Von Hardenberg et al. 2000), and is manifested in the stretching and folding of fluid elements such that vorticity is accumulated into thin sets with sharp gradients. The accumulation of vorticity into these small-scale structures is the embodiment of the downscale enstrophy cascade (Chen et al. 2003), the study of which continues to draw interest due to its relevance to atmospheric and oceanic flows.

The enstrophy cascade itself, being a spectral quantity, is inherently nonlocal and thus challenging to examine in the highly heterogeneous flows of the real ocean. An alternative approach for studying its dynamics instead focuses on the processes governing the production of vorticity gradients, or equivalently the gradients of any tracer which obeys the same evolution equation as vorticity (McWilliams 1984; Weiss 1991; Ohkitani and Kishiba 1995; Protas et al. 1999; Straub 2003).

Regions where the production of gradients is particularly vigorous indicate where the turbulent cascades are especially active, and tend to lie outside the coherent structures associated with large-scale vortices (Mariotti et al. 1994). Methods used to identify vortices thus also implicitly indicate where gradient production is occurring, and by extension where the enstrophy cascade is strongest. These considerations have motivated a sizable body of literature dedicated to partitioning flows into regions that are dominated by strain (gradient-producing) versus those dominated by vorticity. The so-called "Okubo–Weiss parameter" (hereafter W; Okubo 1970; Weiss 1991) is perhaps the most well-known and easily applied criterion to partition ocean flows in this way, and has found many applications due to its facility with both model (e.g., Poje et al. 2010; Williams et al. 2011; Petersen et al. 2013) and altimetric data (e.g., Isern-Fontanet et al. 2003, 2004; Chelton et al. 2007; Henson and Thomas 2008; Souza et al. 2011, among others). It, too, was conceptualized for 2D flows, and its use in physical oceanography is justified largely by the quasi-horizontal nature of mesoscale motions.

Among oceanographers W is perhaps the most familiar solution to a more general problem in fluid dynamics, which is to develop a mathematical criterion with which to identify vortices. Several Eulerian schemes for vortex identification have been proposed in previous literature, many of which, like W, are based on an eigendecomposition of the velocity gradient tensor (e.g., Hunt et al. 1988; Chong et al. 1990; Berdahl and Thompson 1993; Zhou et al. 1999). Essentially all of these schemes are mathematically related to each other (Chakraborty et al. 2005); in fact, the Q criterion of Hunt et al. (1988) is identified as the three-dimensional generalization of W. Even more mathematically rigorous identification schemes have been developed which are invariant under rotations and translations ("objective"; e.g., Haller and Yuan 2000; Haller 2005; Haller et al. 2016), and which are shown to be superior to eigenvalue-based methods for vortex identification in unsteady and chaotic flows (e.g., Serra and Haller 2016; Pedergnana et al. 2020). Such methods are superior in their ability to track the material coherence of eddies, and recent work has shown that they can differ greatly from Eulerian methods in

---

Corresponding author: Scott D. Bachman, bachman@ucar.edu

DOI: 10.1175/JPO-D-21-0037.1

their estimates of ocean eddy transport (e.g., Abernathey and Haller 2018; Tarshish et al. 2018; Liu et al. 2019).

Nonetheless, among all of the available vortex identification schemes, the use of W remains prevalent in physical oceanography due to its simplicity and practicality. It is most commonly applied with altimetric data (e.g., Isern-Fontanet et al. 2003, 2004; Chelton et al. 2007, among others) to study mesoscale eddy characteristics, such as eddy lifetime, propagation distance, and size (e.g., Chelton et al. 2007, 2011). The prominence of mesoscale eddies and the strong tendency of their cores to be vorticity-dominated tends to make W-based detection methods reasonably skillful and quite visually compelling. The use of W as a diagnostic tool is not without shortcomings, however, and simple examples can be constructed where the criterion fails (e.g., Pierrehumbert and Yang 1993; Balmforth et al. 2000). In observational oceanography its primary deficiency, as described by Chelton et al. (2011), is that the geostrophic velocities that are used in its calculation are inferred from the sea surface height field h. The resulting equation for W is a quadratic function of the second derivatives of h, making it highly sensitive to noise in the altimetric data. For the particular application of eddy detection, W-based methods can also have difficulty distinguishing eddies from other strongly vortical features such as jet meanders (e.g., d'Ovidio et al. 2009; Souza et al. 2011; Williams et al. 2011). For these reasons eddy detection methods based on W are frequently employed using additional constraints, such as imposing a user-defined threshold to filter out regions where $|W|$ is small and the flow structures are ambiguous (e.g., Isern-Fontanet et al. 2003; Morrow et al. 2004; Chelton et al. 2007).

This manuscript is partially motivated by the recognition that there are other vorticity-dominated features in the ocean that would not be properly classified as mesoscale eddies, but are nonetheless of dynamical interest. An obvious limitation of W as an ocean diagnostic is that it is purely a function of *horizontal* velocities and derivatives, whereas the ocean's *vertical* shear and circulations drive some of the processes most fundamental to the broader climate system (e.g., Mahadevan and Tandon 2006; Thomas et al. 2008; Klein and Lapeyre 2009; Lévy et al. 2012). At large scales the velocity field is in approximate geostrophic and thermal wind balance, such that the vertical shears can be related to the horizontal derivatives of density via the QG approximation. This suggests an opportunity to explore new vortex identification schemes that have the same practical advantages as W (viz., that they can be diagnosed from surface fields via remote sensing) while still taking the vertical dimension into account. The increasing resolution of gridded observational products pertaining to h (e.g., Taburet et al. 2019; Zlotnicki et al. 2019), sea surface temperature (e.g., Donlon et al. 2012), and sea surface salinity (e.g., Droghei et al. 2018; Reul et al. 2020) means that observing structures smaller than mesoscale eddies is within reach (Reul et al. 2014; Umbert et al. 2015; Isern-Fontanet et al. 2016; Melnichenko et al. 2017; Vinogradova et al. 2019), and will become even more so with future remote sensing missions such as the Surface Water and Ocean Topography (SWOT; Fu et al. 2009), the proposed Copernicus Imaging Microwave Radiometer (CIMR; Kilic et al. 2018), and Soil Moisture and Ocean Salinity–High Resolution (SMOS-HR; Rodríguez-Fernández et al. 2019).

Looking beyond the application of vortex identification, the dynamics also provide motivation to explore new methods for separating strain- and rotation-dominated parts of the flow. Partitioning the flow in this way can yield information about which parts of the ocean favor vigorous turbulent cascades or are conduits for ocean ventilation (e.g., Klocker 2018; Bachman and Klocker 2020; Balwada et al. 2021), as well as their unique roles in the ocean energy cycle (e.g., Ferrari and Wunsch 2009, 2010; Storch et al. 2012; Chen et al. 2014). Part of the approach here is to take a critical look at the use of W in this context and to evaluate how it might fail, and alternatively, to consider whether any of the other previously mentioned schemes are better suited for exploring these topics. Last, the inclusion of the vertical dimension allows us to consider what geometric properties of these flow structures can be inferred from just the surface fields.

The purpose of this manuscript is to develop alternative Eulerian diagnostics to W that retain its appealing mathematical simplicity and applicability with surface diagnostics, while including dynamics associated with the vertical dimension. As such, the approach here begins by considering a QG flow, as opposed to the 2D framework typically used for W. Like many of the extant schemes mentioned above, the mathematics will involve an eigenanalysis based on decomposing the velocity gradient tensor, so that the results can be understood both algebraically (via eigenvalues) and geometrically (via eigenvectors).

The remainder of this paper is laid out as follows. Section 2 will review the mathematical concepts behind the Okubo–Weiss approach and why it becomes a degenerate mathematical problem in QG. An alternative approach based on the λ_2 criterion (Jeong and Hussain 1995) will be presented, and will be analyzed via the eigenvalues and eigenvectors of the associated tensor. Section 4 will present diagnoses of the resulting parameters (both 2D and QG) from realistic numerical simulations. Concluding remarks appear in section 5.

2. The Okubo–Weiss approach for 2D and QG flows

a. The velocity gradient, strain-rate, and vorticity tensors

As this study will examine both two- and three-dimensional (QG) flows, this introductory discussion will establish the mathematical underpinnings of the Okubo–Weiss parameter in the 2D case before examining why this approach becomes degenerate in QG. Unlike the original derivations by Okubo (1970) and Weiss (1991), here the dynamics will be considered in the rotating frame to make the role of the Coriolis force explicit. For simplicity the motion will be considered on the f plane (which in the context of W is appropriate since it is entirely based on local velocity gradients) with constant Coriolis parameter f_0, though it is possible to generalize these arguments to cases where f varies meridionally as well (Hua et al. 1998).

The underlying concept of the Okubo–Weiss parameter is to consider whether a flow is more likely to stretch and strain fluid elements, or to simply rotate them in the absence of deformation. The tendency of a flow to perform these actions is reflected in the way the velocity field varies in space, which is given mathematically by the velocity gradient tensor,

$$\nabla \mathbf{u} = \partial_j u_i, \tag{1}$$

where i indicates the row and j indicates the column. The symmetric and antisymmetric parts of the velocity gradient tensor are known as the strain-rate (rate of deformation) tensor $\mathbf{S}$ and vorticity (spin) tensor $\boldsymbol{\Omega}$, respectively, which are easily calculated via $\nabla \mathbf{u}$ and its transpose, $\nabla \mathbf{u}^{\mathrm{T}}$. Mathematically they are identified as

$$\nabla \mathbf{u} = \mathbf{S} + \boldsymbol{\Omega}, \tag{2}$$

$$\mathbf{S} = \frac{1}{2}(\nabla \mathbf{u} + \nabla \mathbf{u}^{\mathrm{T}}), \tag{3}$$

$$\boldsymbol{\Omega} = \frac{1}{2}(\nabla \mathbf{u} - \nabla \mathbf{u}^{\mathrm{T}}). \tag{4}$$

The evolution of the strain-rate and vorticity tensors can be obtained by taking the gradient of the momentum equations, here written in a general form for both 2D and QG flows as

$$\frac{D\mathbf{u}}{Dt} = -\mathscr{F} - \nabla \phi + \nu \nabla^2 \mathbf{u}, \tag{5}$$

for an incompressible velocity field $\mathbf{u} = (u, v)$, Coriolis term $\mathscr{F}$, pressure potential φ, constant viscosity ν, and material derivative $D/Dt = \partial t + u\partial_x + v\partial_y$. The gradient of (5) can then be split into symmetric and antisymmetric parts to obtain evolution equations for $\mathbf{S}$ and $\boldsymbol{\Omega}$,

$$\frac{D\mathbf{S}}{Dt} = -\mathbf{S}^2 - \boldsymbol{\Omega}^2 - \mathscr{F}_{\mathbf{S}} - \phi'' + \nu \nabla^2 \mathbf{S}, \tag{6}$$

$$\frac{D\boldsymbol{\Omega}}{Dt} = -\mathbf{S}\boldsymbol{\Omega} - \boldsymbol{\Omega}\mathbf{S} - \mathscr{F}_{\boldsymbol{\Omega}} + \nu \nabla^2 \boldsymbol{\Omega}, \tag{7}$$

where the subscripts on $\mathscr{F}$ indicate the decomposition of the Coriolis term. The nonlinear terms immediately to the right of the equal signs arise from applying the gradient operator to the advection terms inside the material derivative. The term ϕ'' is known as the pressure Hessian, which has historically played a central role in studies of vortex identification and gradient formation in incompressible flows (e.g., Jeong and Hussain 1995; Hua and Klein 1998; Chevillard et al. 2008). Note that convenient simplifications to (7) can be made for 2D flow since in this special case $\mathbf{S}\boldsymbol{\Omega} + \boldsymbol{\Omega}\mathbf{S}$ and $\mathscr{F}_{\boldsymbol{\Omega}} = 0$. The evolution equation for $\boldsymbol{\Omega}$ thus reduces to the familiar identity that for inviscid flow the vorticity is conserved along Lagrangian trajectories.

As a final introductory step before deriving the Okubo–Weiss parameter, note that for two-dimensional flow the tensors $\mathbf{S}$ and $\boldsymbol{\Omega}$ can be expressed as

$$\mathbf{S} = \frac{1}{2}\begin{bmatrix} \sigma_n & \sigma_s \\ \sigma_s & -\sigma_n \end{bmatrix} \quad \text{and} \quad \boldsymbol{\Omega} = \frac{1}{2}\begin{bmatrix} 0 & -\omega \\ \omega & 0 \end{bmatrix}, \tag{8}$$

using the normal strain, $\sigma_n = \partial_x u - \partial_y v$, shearing strain, $\sigma_s = \partial_x v + \partial_y u$, and relative vorticity, $\omega = \partial_x v - \partial_y u$.

b. The 2D tracer gradient problem

The derivation of W in the 2D problem begins by either considering the evolution of particle trajectories (e.g., Okubo 1970) or tracer gradients (e.g., Weiss 1991), which are essentially dual approaches that yield the same overall interpretation (Hua and Klein 1998). Here the analysis will focus on the tracer gradient problem, and in particular we will consider a conserved tracer q. The choice to name this tracer q is done purposefully to evoke that these derivations also apply when considering the absolute vorticity (2D) or potential vorticity (QG) on the f plane, both of which are conserved in their respective flow regimes and are often denoted by q in the oceanographic literature.

The evolution of the gradient of q along a Lagrangian trajectory is given by

$$\frac{D\nabla q}{Dt} = -\nabla \mathbf{u}^{\mathrm{T}} \nabla q. \tag{9}$$

This is a set of coupled partial differential equations for the elements of the vector ∇q, where the coupling coefficients are the elements of $\nabla \mathbf{u}^{\mathrm{T}}$ and vary in both time and space. In the standard derivation of W one assumes that the elements of $\nabla \mathbf{u}^{\mathrm{T}}$ evolve slowly in comparison to ∇q,[1] in which case (9) can be approximated as a linear set of ordinary differential equations (ODEs) in t with constant coefficients. The general solution for this problem is a linear combination of the eigenvalues and eigenvectors of $\nabla \mathbf{u}^{\mathrm{T}}$, with the eigenvalues depicting the nature of the velocity field and the eigenvectors governing the rate of change depending on their alignment with ∇q (more on this below). Both Okubo (1970) and Weiss (1991) focused on the eigenvalues λ, showing that they are roots of the characteristic equation

$$\lambda^2 = \frac{1}{4}(\sigma^2 - \omega^2), \tag{10}$$

where $\sigma^2 = \sigma_n^2 + \sigma_s^2$ is the square of the total deformation. The Okubo–Weiss parameter is given by the expression in (10) bracketed by parentheses,

$$W = \sigma^2 - \omega^2. \tag{11}$$

When W is positive, strain dominates over vorticity, the eigenvalues of $\nabla \mathbf{u}^{\mathrm{T}}$ are real, and the general solution of (9) predicts exponential growth of ∇q in time. When it is negative, the vorticity dominates over the strain, the eigenvalues are purely complex, and the solution of (9) predicts orbital motion that neither grows or decays in time. In this sense negative values of W evoke what one might imagine to be the behavior of a vortex, where the orientation of the tracer gradient merely gets rotated by the vortical flow without changing in magnitude.

Another way to analyze this problem is through the gradient norm equation, which is derived by taking the dot product of (9) with ∇q and can be written

$$\frac{D|\nabla q|^2}{Dt} = -2\nabla q^{\mathrm{T}} \mathbf{S} \nabla q. \tag{12}$$

---

[1] Note that this assumption was shown by Basdevant and Philipovitch (1994) to generally not hold except in vortex cores.

A salient property of this equation is that, unlike in (9) where the full velocity gradient tensor affects the dynamics, the change in the gradient norm only depends on the strain-rate tensor $\mathbf{S}$. Note that this equation is derived without making any assumptions about whether $\mathbf{S}$ varies slowly, but the dynamics are broadly consistent with what the Okubo–Weiss method predicts. For example, supposing that $\boldsymbol{\Omega}_{ij} \gg \mathbf{S}_{ij}$ for all i and j so that one can replace $\nabla \mathbf{u}^{\mathrm{T}}$ with $\boldsymbol{\Omega}$ in (9), one would obtain that the right hand side of (12) would be zero and the gradient norm would not change following the motion. Alternatively, one can make the assumption $\mathbf{S}_{ij} \gg \boldsymbol{\Omega}_{ij}$ for all i and j, the results of which are most easily shown by rotating the coordinate system into a frame that is aligned with the eigenvectors of $\mathbf{S}$ (the strain basis). To do so, one can define a rotation matrix $\mathscr{R}(\theta)$ that rotates the coordinate axes by an angle

$$\theta = \frac{1}{2}\tan^{-1}\left(\frac{\sigma_s}{\sigma_n}\right). \tag{13}$$

With this transformation one can define a new vector $\mathbf{Y}$, such that $\nabla q = \mathscr{R}(\theta)\mathbf{Y}$, which gives

$$\frac{D|\mathbf{Y}|^2}{Dt} = -2[\mathscr{R}(\theta)\mathbf{Y}]^{\mathrm{T}}\mathbf{S}\mathscr{R}(\theta)\mathbf{Y}, \tag{14}$$

$$= -2\mathbf{Y}^{\mathrm{T}}\mathscr{R}(\theta)^{\mathrm{T}}\mathbf{S}\mathscr{R}(\theta)\mathbf{Y}, \tag{15}$$

$$= -\mathbf{Y}^{\mathrm{T}}\boldsymbol{\Sigma}\mathbf{Y}, \tag{16}$$

where

$$\boldsymbol{\Sigma} = \begin{pmatrix} \sigma & 0 \\ 0 & -\sigma \end{pmatrix} \tag{17}$$

is a diagonal matrix of the eigenvalues of $\mathbf{S}$ (or equivalently, the strain-rate tensor written in the strain basis). Writing $\mathbf{Y} = (y_1, y_2)$, (16) can be rewritten as

$$\frac{D|\mathbf{Y}|^2}{Dt} = -\sigma(y_1^2 - y_2^2), \tag{18}$$

which shows that the tendency of the gradient norm depends on both the magnitude of the strain and its orientation. The latter is an aspect of the tracer gradient dynamics that the Okubo–Weiss approach ignores. Equation (18) makes it clear that the change of the gradient norm depends on the alignment of $\mathbf{Y}$ with the axes of the strain basis. The growth of the norm is maximized if $\mathbf{Y} = (0, 1)$, wherein the tracer gradient is aligned with the eigenvector $\mathbf{e}_2 = (0,1)$ (the compressional axis) for the negative eigenvalue of $\mathbf{S}$. The norm neither grows or decays if $\mathbf{Y} = (1, 1)$, which would be aligned with the bisector of the strain-rate eigenvectors (e.g., Lapeyre et al. 1999; Klein et al. 2000). The decay of the norm is maximized if $\mathbf{Y} = (1, 0)$, aligned with the eigenvector $\mathbf{e}_1 = (1, 0)$ (the extensional axis) of the positive eigenvalue. For a visual depiction of this geometry the reader is encouraged to consult Fig. 1 of Klein et al. (2000). Note that if one assumes that the strain rate varies slowly compared to $\mathbf{Y}$, i.e., the same assumption as used for the Okubo–Weiss derivation, (18) predicts exponential growth (decay) of the norm if the tracer gradient is aligned with $\mathbf{e}_2$ ($\mathbf{e}_1$).

A key point here is that both unique elements of the strain-rate tensor (σ_n and σ_s) appear in the growth rate for the gradient norm. The Okubo–Weiss parameter for 2D flows is thus consistent in the sense that it is completely described by the elements of $\mathbf{S}$ and $\boldsymbol{\Omega}$; that is, there are no components of the strain-rate or vorticity tensors that are not accounted for in the expression for W. It will next be shown that this is not the case for the QG problem, requiring deeper consideration of how to measure the competition between strain and vorticity in QG flows.

c. *The degeneracy of the QG tracer gradient problem*

In QG the evolution of the gradient of q along a Lagrangian trajectory is still given by (9), except that the problem now involves three dimensions so that

$$\nabla \mathbf{u}_{\mathrm{QG}}^{\mathrm{T}} = \begin{pmatrix} u_x & v_x & 0 \\ u_y & v_y & 0 \\ u_z & v_z & 0 \end{pmatrix}. \tag{19}$$

Note that the third column is zero because in QG the vertical velocity in the advection operator is asymptotically small. Following the same procedure as for the 2D case, one assumes that the elements of $\nabla \mathbf{u}_{\mathrm{QG}}^{\mathrm{T}}$ evolve slowly compared to ∇q, yielding a system of coupled linear ODEs whose solution is given by the eigenvalues and eigenvectors of $\nabla \mathbf{u}_{\mathrm{QG}}^{\mathrm{T}}$. The eigenvalues of $\nabla \mathbf{u}_{\mathrm{QG}}^{\mathrm{T}}$ are $\lambda = 0, \quad \pm(1/2)(\sigma^2 - \omega^2)^{1/2}$, with the zero eigenvalue corresponding to the vertical eigenvector, $\mathbf{e}_3 = (0, 0, 1)$. One readily notices that the nonzero eigenvalues are the same as for the 2D problem.

That the 2D and QG velocity gradient tensors have the same nonzero eigenvalues suggests that W remains a useful metric for QG flows. However, examination of the gradient norm problem [introduced for the 2D case in (12)] reveals an important difference. As was the case for the tracer gradient problem (9), the QG version of the gradient norm problem also shares the same mathematical form as in the 2D case, but instead uses the QG strain-rate tensor

$$\mathbf{S}_{\mathrm{QG}} = \frac{1}{2}\begin{pmatrix} \sigma_n & \sigma_s & u_z \\ \sigma_s & -\sigma_n & v_z \\ u_z & v_z & 0 \end{pmatrix}. \tag{20}$$

It is immediately clear that $\mathbf{S}_{\mathrm{QG}}$ contains elements related to the vertical geostrophic shear, u_z and v_z, which are not accounted for in W. Taking this point further, one can easily create a pathological example wherein the vertical shear is the *only* relevant parameter in the gradient norm problem. For example, consider a purely zonal flow whose only spatial variations are in the vertical direction, so that u_z is the only nonzero element of $\mathbf{S}_{\mathrm{QG}}$. One can then follow an analogous procedure as in (13)–(18), where this time a counterclockwise rotation of 45° about the y axis is sufficient to rotate the coordinate frame into the strain basis and diagonalize $\mathbf{S}_{\mathrm{QG}}$. Writing $\mathbf{Y} = (y_1, y_2, y_3)$, the analogous equation to (18) is

$$\frac{D|\mathbf{Y}|^2}{Dt} = -u_z(y_1^2 - y_3^2). \tag{21}$$

The zonal vertical shear u_z here plays the same role as did σ in (18), modulating the rate of change of the gradient norm independent of the gradient's orientation. Crucially, it confirms that the component of the strain-rate tensor associated with the vertical shear should be accounted for by any parameter aiming to categorize strain-vorticity dynamics in QG. The 2D Okubo–Weiss parameter does not satisfy this requirement, as it measures only the horizontal components of the strain.

That the eigenvalues of $\nabla\mathbf{u}_{\mathrm{QG}}^{\mathrm{T}}$ lack any information about the vertical shear is an example of the "degenerate dynamics of particle stirring" at leading order for QG flows (cf. Hua et al. 1998). This use of the adjective "degenerate" refers to mathematical degeneracy, in which the dimensionality of the solution to (9) is reduced. In this context it means that the QG version of (9) is a three-dimensional problem, but its solution is effectively only 2D since the third (vertical) eigenvalue is zero. Both Hua et al. (1998) and Smith and Ferrari (2009) show that the degeneracy arises because of a peculiarity in the dynamics of the QG tracer gradient problem, which is that the vertical gradient depends on the strength of the horizontal gradient but not vice versa. Because the Okubo–Weiss approach assesses the horizontal and vertical gradients jointly it is unaware of this degeneracy and only detects the horizontal dynamics as being important.

The use of W in QG flows (here taken as synonymous with real ocean mesoscale flows) thus misses the vertical shears that are crucial in both the QG strain-rate tensor, (20), and vorticity tensor,

$$\boldsymbol{\Omega}_{\mathrm{QG}} = \frac{1}{2}\begin{pmatrix} 0 & -\omega & u_z \\ \omega & 0 & v_z \\ -u_z & -v_z & 0 \end{pmatrix}. \tag{22}$$

It is this degeneracy that motivates the effort in this paper, which is to develop an alternative Eulerian method to W for use in large-scale oceanography. Many of the candidate vortex identification parameters mentioned in the Introduction (e.g., Hunt et al. 1988; Chong et al. 1990; Berdahl and Thompson 1993; Zhou et al. 1999) are immediately disqualified on the basis that they are also informed by the eigenvalues of $\nabla\mathbf{u}_{\mathrm{QG}}^{\mathrm{T}}$. That is, none of these parameters will overcome the degeneracy that afflicts W in QG. Others involve a level of mathematical sophistication that is likely beyond the needs or capabilities of typical oceanographic applications.[2] The next section will highlight one scheme, the λ_2 criterion proposed by Jeong and Hussain (1995), as a promising way to avoid the degeneracy of the above schemes despite its mathematical connection with W.

3. The λ_2 criterion for QG flows

Before discussing the merits of the λ_2 criterion, it is useful to list some desirable properties that a vortex identification scheme should possess when used for QG flows. Note that this discussion will only pertain to Eulerian schemes based on velocity gradients and their constituent tensors (2)–(4), so approaches using methods such as streamline computation (e.g., Sadarjoen and Post 2000; Nencioli et al. 2010) or Lagrangian descriptors (e.g., Madrid and Mancho 2009; Mancho et al. 2013) will not be considered.

It is important to recognize that the family of schemes based on measuring the eigenvalues of $\nabla\mathbf{u}_{\mathrm{QG}}^{\mathrm{T}}$ (which includes W) is both well recognized and highly successful. Though the new scheme does not necessarily have to follow this exact approach, the velocity gradient tensor (2) does serve as a mathematical common ground for an even broader array of schemes (Chakraborty et al. 2005). Given the dynamical and mathematical similarities between 2D and QG flows, it is thus not unreasonable to expect that the new QG scheme should exhibit some connections with its 2D counterpart. In particular, we will use W as a sort of "baseline scheme" in this discussion, such that for the QG scheme the following properties are desired:

- The scheme should somehow manifest the standard (2D) definition of W if $\mathbf{u}_z = 0$.
- The parameters obtained through the scheme must be real, i.e., the eigenvalues of a symmetric tensor.
- The small aspect ratio of QG flows means that the relevant strain and vorticity dynamics are quasi-horizontal. The tensor that yields these new parameters should have eigenvectors that reflect this quasi-horizontal geometry.

These criteria essentially insist that this scheme is treated as an extension of a 2D problem, in that purely 2D dynamics are recovered in the limit of no vertical shear. This section will introduce the λ_2 criterion as a scheme that satisfies these criteria. It was previously applied to a QG flow by Petersen et al. (2006) to identify vortices in an idealized domain, but was not examined in terms of its geometric properties. These properties will be one of the focal points here.

The λ_2 criterion was originally derived by Jeong and Hussain (1995), who insisted that for an object to be considered a vortex it must have a net circulation and it must be Galilean invariant. They noted that many extant vortex definitions (pressure minima, closed streamlines, and surfaces of constant vorticity) fail to meet these criteria even in relatively well-understood flows. In particular, they sought to avoid scenarios where pressure minima occurred without vortical motion and, conversely, where vortical motion occurred but the pressure minima were destroyed by other effects such as viscosity. To that end, they proposed ignoring all terms in the strain-rate equation (6) except for the nonlinear terms $\mathbf{S}^2 + \boldsymbol{\Omega}^2$ and the pressure Hessian, so that the topology of the pressure field would be directly associated with the local strain and vorticity fields. Their rationale was that, by isolating the effects of the local velocity gradients on the pressure field, a vortex would unambiguously correspond to a pressure minimum. This would occur when ϕ'' has two negative eigenvalues, or by the above assumption, when $\mathbf{S}^2 + \boldsymbol{\Omega}^2$ has two negative eigenvalues, permitting analysis akin to the Okubo–Weiss approach where the nature of the flow depends on the local velocity gradients. Note that the moniker "λ_2" refers to the critical role the second eigenvalue plays in this framework, as it is simple to see that if one sorts the eigenvalues of $\mathbf{S}^2 + \boldsymbol{\Omega}^2$ such that $\lambda_1 \geq \lambda_2 \geq \lambda_3$, the sign of λ_2 is sufficient to determine whether an object is a vortex or not.

---

[2] The author notes that the criterion introduced by Haller (2005) requires no mathematics beyond what will be used in this paper, and thus would be an intriguing target for future work that is both sophisticated and accessible.

It is notable that the λ_2 criterion applies to both 2D and 3D flows. In fact, in 2D the relationship between the Okubo–Weiss and λ_2 approaches is quite explicit, since

$$\mathbf{S}^2 + \mathbf{\Omega}^2 = \frac{1}{4}\begin{pmatrix} W & 0 \\ 0 & W \end{pmatrix} \tag{23}$$

is a symmetric tensor with a double eigenvalue, $W/4$. This tensor thus has two negative eigenvalues when $W < 0$, which is associated with a vortex according to both the λ_2 and Okubo–Weiss criteria.

The QG version of this tensor is more interesting, and can be written

$$\mathbf{S}^2_{\mathrm{QG}} + \mathbf{\Omega}^2_{\mathrm{QG}} = \frac{1}{4}\begin{pmatrix} \sigma^2 - \omega^2 & 0 & \sigma_n u_z + \sigma_s v_z - \omega v_z \\ 0 & \sigma^2 - \omega^2 & \sigma_s u_z + \omega u_z - \sigma_n v_z \\ \sigma_n u_z + \sigma_s v_z - \omega v_z & \sigma_s u_z + \omega u_z - \sigma_n v_z & 0 \end{pmatrix} \tag{24}$$

$$= \frac{1}{4}\begin{pmatrix} W & 0 & -\dfrac{2}{f_0}Q_2 \\ 0 & W & \dfrac{2}{f_0}Q_1 \\ -\dfrac{2}{f_0}Q_2 & \dfrac{2}{f_0}Q_1 & 0 \end{pmatrix}. \tag{25}$$

The second, more succinct, equality in (25) employs thermal wind balance,

$$f_0 \hat{\mathbf{k}} \times \partial_z \mathbf{u} = -\nabla_h b, \tag{26}$$

to introduce the quasigeostrophic $\mathbf{Q}$ vector, $\mathbf{Q} = (Q_1, Q_2) = (-\mathbf{u}_x \cdot \nabla_h b, -\mathbf{u}_y \cdot \nabla_h b)$ (Hoskins et al. 1978), where $\nabla_h = (\partial_x, \partial_y)$ and b is the buoyancy. The eigenvalues of $\mathbf{S}^2_{\mathrm{QG}} + \mathbf{\Omega}^2_{\mathrm{QG}}$, written from largest to smallest and labeled such that $\lambda_1 \geq \lambda_2 \geq \lambda_3$, are (Petersen et al. 2006):

$$\lambda_1 = \frac{1}{2}\left(\frac{1}{4}W\right) + \frac{1}{2}\sqrt{\left(\frac{1}{4}W\right)^2 + \frac{|\mathbf{Q}|^2}{f_0^2}}, \tag{27}$$

$$\lambda_2 = \frac{1}{4}W, \tag{28}$$

$$\lambda_3 = \frac{1}{2}\left(\frac{1}{4}W\right) - \frac{1}{2}\sqrt{\left(\frac{1}{4}W\right)^2 + \frac{|\mathbf{Q}|^2}{f_0^2}}. \tag{29}$$

Simple inspection reveals that, as long as $|\mathbf{Q}|$ is nonzero, λ_1 is always positive, λ_3 is always negative, and the sign of λ_2 is the same as the sign of W.[3] Notably, the magnitudes of λ_1 and λ_3 are asymmetric about zero, with the asymmetry determined by the sign of W: if $W < 0$ then $|\lambda_3| > |\lambda_1|$, and vice versa if $W > 0$.

Before proceeding further it is worth examining the key features of (25) and whether they satisfy the desired bullet points at the beginning of this section. First, it is clear that this tensor is symmetric and its eigenvalues are thus guaranteed to be real. In the limit where $\mathbf{u}_z = 0$ the tensor as a whole reduces to the 2D version in (23), with zeros in the third row and column. It is thus perhaps unsurprising that, in similar fashion to (23), its eigenvalues reflect the influence of W. The final bullet point requires a derivation of the eigenvectors, and will make use of the asymmetry of the eigenvalues noted above.

a. The geometry of $\mathbf{S}^2_{\mathrm{QG}} + \mathbf{\Omega}^2_{\mathrm{QG}}$

For an arbitrary scalar field the Hessian matrix is a matrix of second derivatives that describes the curvature, or topology, of the field. Because the Hessian is symmetric its eigenvectors are orthogonal, and so its axes form a coordinate system with which to naturally describe the geometry of the field. In using the approach of the λ_2 criterion, setting $\mathbf{S}^2_{\mathrm{QG}} + \mathbf{\Omega}^2_{\mathrm{QG}}$ equal to the pressure Hessian means that the topology of the pressure field is described by the eigenvectors of $\mathbf{S}^2_{\mathrm{QG}} + \mathbf{\Omega}^2_{\mathrm{QG}}$. When $\mathbf{S}^2_{\mathrm{QG}} + \mathbf{\Omega}^2_{\mathrm{QG}}$ has two negative eigenvalues the pressure field therefore has a minimum in the plane spanned by the corresponding eigenvectors, and a vortex rotating in this plane has its axis aligned with the third eigenvector.

Here the eigenvectors of $\mathbf{S}^2_{\mathrm{QG}} + \mathbf{\Omega}^2_{\mathrm{QG}}$ will be denoted $\mathbf{e}_i$ for $i = \{1,2,3\}$, with the subscript indices matching those of the corresponding eigenvalues (27)–(29). Using standard linear algebra techniques, it is straightforward to show that

$$\mathbf{e}_1 = \begin{pmatrix} \dfrac{1}{2}\dfrac{Q_2}{f_0} \\ -\dfrac{1}{2}\dfrac{Q_1}{f_0} \\ \lambda_3 \end{pmatrix}, \quad \mathbf{e}_2 = \begin{pmatrix} Q_1 \\ Q_2 \\ 0 \end{pmatrix}, \quad \mathbf{e}_3 = \begin{pmatrix} \dfrac{1}{2}\dfrac{Q_2}{f_0} \\ -\dfrac{1}{2}\dfrac{Q_1}{f_0} \\ \lambda_1 \end{pmatrix}. \tag{30}$$

A few points are worth noting regarding these eigenvectors. First, $\mathbf{e}_2$ is always strictly horizontal and is aligned with $\mathbf{Q}$. By the orthogonality of the eigenvectors, $\mathbf{e}_1$ and $\mathbf{e}_3$ are thus tilted with respect to the horizontal and their projections onto the horizontal plane lie perpendicular to $\mathbf{Q}$. The angles formed between the horizontal plane and $\mathbf{e}_1$ and $\mathbf{e}_3$ thus indicate the tilt of the resulting flow structures: when $\lambda_2 < 0$ a pressure minimum occurs in the plane spanned by $\mathbf{e}_2$ and $\mathbf{e}_3$, and the axis of the resulting vortex is given by $n_- = \mathbf{e}_2 \times \mathbf{e}_3$ and is parallel with $\mathbf{e}_1$. Conversely, when $\lambda_2 > 0$ a pressure maximum occurs in the

---

[3] The signs of the eigenvalues retain this property even for general 3D flows. The "λ_2" moniker of the criterion thus alludes to the fact that the occurrence of a vortex hinges entirely on the sign of λ_2, or in the 2D and QG cases, the sign of W (Petersen et al. 2006).

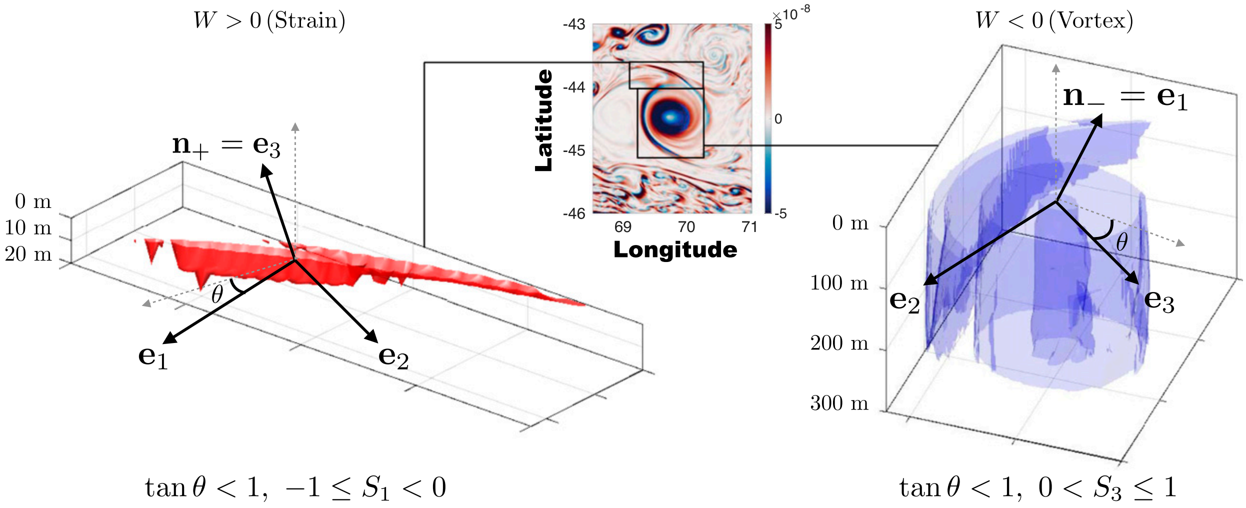

FIG. 1. Schematic showing the tilt of the principal axes of $\mathbf{S}_{\mathrm{QG}}^2 + \mathbf{\Omega}_{\mathrm{QG}}^2$ for (left) strain and (right) vortex structures. The coordinate axes are shown by the dashed gray lines. Eigenvector $\mathbf{e}_2$ is always horizontal. The angle between the horizontal plane and the plane parallel to the pressure extremum is given by θ.

plane spanned by $\mathbf{e}_2$ and $\mathbf{e}_1$, and the axis of the strain field is $n_+ = \mathbf{e}_1 \times \mathbf{e}_2$ and is parallel with $\mathbf{e}_3$. Since $\mathbf{e}_2$ is purely horizontal the tilt of the vortex or strain field is given by the slope of the accompanying vector, $\mathbf{e}_3$ or $\mathbf{e}_1$, for cases when $\lambda_2 < 0$ and $\lambda_2 > 0$, respectively. A schematic depiction of these results appears in Fig. 1, which are also summarized in Table 1.

The slope of this vector can be calculated as the vector's vertical component divided by the Euclidean norm of its horizontal components. Using the identity

$$\lambda_1\lambda_3 = -\frac{1}{4}\frac{|\mathbf{Q}|^2}{f_0^2}, \tag{31}$$

the slope of $\mathbf{e}_1$ is

$$S_1 = \frac{\lambda_3}{\sqrt{-\lambda_1\lambda_3}} = -\sqrt{-\frac{\lambda_3}{\lambda_1}} < 0, \tag{32}$$

and, likewise, it can readily be shown that the slope of $\mathbf{e}_3$ is

$$S_3 = \sqrt{-\frac{\lambda_1}{\lambda_3}} > 0. \tag{33}$$

Here we return to the earlier point that λ_1 and λ_3 are asymmetric about zero, and that the eigenvalue with the larger magnitude is the one that shares the same sign as W (or λ_2). When $\lambda_1 < 0$ the tilt of the resulting vortex is given by S_3, and since in this case $|\lambda_3| \ge |\lambda_1|$, by (33) this establishes the bounds $0 < S_3 \le 1$. An analogous effect occurs when strain dominates: $\lambda_2 > 0$ implies that the slope of the strain field is given by S_1, and since $|\lambda_1| \ge |\lambda_3|$ a bound emerges that $-1 \le S_1 < 0$. When $W = 0$ we reach the limiting case where $S_1 = 1$ and $S_3 = 1$. The eigenvectors of $\mathbf{S}_{\mathrm{QG}}^2 + \mathbf{\Omega}_{\mathrm{QG}}^2$ are thus oriented so that the dominant flow structure (vortex or strain) has a slope that is bounded in magnitude by one, so that its tilt is more horizontal than vertical. These rules regarding the slope of the eigenvectors always remain valid for QG flows except in the singular limit $\mathbf{u}_z = 0$. These results affirm the final bullet point at the beginning of this section, which is that the flow structures in QG should exhibit quasi-horizontal geometry.

One final interesting property of these eigenvectors is worth noting, which is that they can be used to diagnose the relative importance of the baroclinicity in setting the curvature of the pressure field. Consider the case of a vortex, so that $W < 0$ and the tilt of the vortex is given by S_3. Using (31), one may rewrite (33) in the form

$$\Pi_3 \equiv S_3 | W < 0 = \frac{|f_0|W}{4|\mathbf{Q}|} + \sqrt{\left(\frac{|f_0|W}{4|\mathbf{Q}|}\right)^2 + 1}, \tag{34}$$

where the new variable, Π_3, has been defined to indicate that we are only considering S_3 for vortex-dominated flows. Rewriting (33) in this way allows us to anticipate the behavior of Π_3 for different values of W and $|\mathbf{Q}|$. To begin, note that the first term on the right side of (34) is negative, the term involving the square root is positive, and thus $0 < \Pi_3 \le 1$. In the limit where $|W| \ll |\mathbf{Q}|/|f_0|$, when the eigenvalues λ_1 and λ_3 are dominated by the baroclinic term involving $|\mathbf{Q}|$, we would expect $\Pi_3 \approx 1$. Conversely, when $|W| \gg |\mathbf{Q}|/|f_0|$, then λ_1 converges to 0 while λ_3 does not, and so $\Pi_3 \approx 0$. These limits are also reflected in the structure of $\mathbf{S}_{\mathrm{QG}}^2 + \mathbf{\Omega}_{\mathrm{QG}}^2$; when $\Pi_3 \approx 1$ the structure of the tensor is dominated by the off-diagonal terms, and when $\Pi_3 \approx 0$ it

TABLE 1. Summary of the eigendecomposition and geometry for each flow type.

Type	λ_1	λ_2	λ_3	Normal vector	Slope of plane
Strain	+	+	−	$\mathbf{n}_+ = \mathbf{e}_3$	$S_1 = -\sqrt{(-\lambda_3/\lambda_1)} \ge -1$
Vortex	+	−	−	$\mathbf{n}_- = \mathbf{e}_1$	$S_3 = \sqrt{(-\lambda_1/\lambda_3)} \le 1$

essentially takes on the structure of a 2D diagonal matrix with zeros in the third row and column.

An analogous expression can also be derived for a strain field with $W > 0$, whose tilt is given by S_1. In this case we use (32) to define

$$\Pi_1 \equiv S_1 | W > 0 = \frac{|f_0|W}{4|\mathbf{Q}|} - \sqrt{\left(\frac{|f_0|W}{4|\mathbf{Q}|}\right)^2 + 1}, \qquad (35)$$

which is bounded such that $1 \le \Pi_3 < 0$. A similar result as above is obtained: when $|W| \ll |\mathbf{Q}|/|f_0|$ we expect $\Pi_1 \approx -1$, and when $|W| \gg |\mathbf{Q}|/|f_0|$ then $\Pi_1 \approx 0$. It is thus clear that both vortices and strain fields are most steeply tilted when the $|\mathbf{Q}|$ term dominates $|W|$, and are essentially horizontal when $|W|$ dominates the $|\mathbf{Q}|$ term.

b. A geometrically motivated extension of the Okubo–Weiss parameter

For real oceanic flows the λ_2 criterion possesses some interesting advantages over the Okubo–Weiss approach, and by the previous subsections these are intrinsically related to the geometry of the flow and its pressure field. As argued earlier, the most important feature of the λ_2 criterion for QG flows is that it accounts for the vertical shear, whose effects are missing in the standard Okubo–Weiss parameter. The cost of these advantages is added complexity–instead of having a single parameter W to identify vortices and quantify their strength, there are now three eigenvalues of $\mathbf{S}_{\mathrm{QG}}^2 + \mathbf{\Omega}_{\mathrm{QG}}^2$ that contain information about both strength and orientation. In this section we explore whether a sensible extension to W can be distilled from these eigenvalues and cast as a single parameter, so as to combine the simplicity of the Okubo–Weiss approach with the geometric advantages of the λ_2 criterion.

For the sake of simply identifying vortices the λ_2 criterion is exactly as straightforward as the Okubo–Weiss parameter, where a structure is a ''vortex'' purely based on the sign of λ_2 (or W). However, λ_2 alone is an insufficient descriptor of the strength of these flow structures since it fails to account for the $\mathbf{Q}$ terms in the other eigenvalues. Put another way, since the whole point of the λ_2 criterion is to describe the curvature of the pressure field, omitting the other eigenvalues is akin to ignoring the direction with greater curvature. Ideally, a single parameter would exist that would retain the simplicity of identifying eddies based purely on the parameter's sign, while still accounting for the contributions of $\mathbf{Q}$. As before, it would be optimal if this parameter (hereafter labeled W^*) reduces to W in the limit of no vertical shear, or alternatively if it could be expressed in an analogous way for both $\mathbf{S}^2 + \mathbf{\Omega}^2$ in the 2D problem and $\mathbf{S}_{\mathrm{QG}}^2 + \mathbf{\Omega}_{\mathrm{QG}}^2$ for the QG problem.

Since no obvious choice for such a parameter emerges from the tensors or their geometry, one must construct the parameter using a combination of mathematical and physical insight. One possibility that was considered for W^* was to use the determinant of $\mathbf{S}_{\mathrm{QG}}^2 + \mathbf{\Omega}_{\mathrm{QG}}^2$, which is the product of its eigenvalues. At first glance this choice seems both convenient and logical—simple inspection of (23) reveals that its square root returns W for the 2D problem, its cube root retains the correct sign of λ_2 for the QG problem, its expression in QG is both uncomplicated and clearly dependent on $\mathbf{Q}$, and also is appealing from a physics perspective since the determinant has well-known geometric properties (Peng 2007). However, the disadvantages of this choice are subtle but critical. The square root of the determinant in the 2D problem has two possibilities for its sign, which is a problem that is easily overcome but still bothersome. More importantly, for the QG problem in the limit where $\mathbf{u}_z = 0$ the determinant is zero. This means that a purely horizontal vortex cannot be measured using this definition of W^*, and so the QG version of this parameter does not cleanly reduce to the 2D version. This potential definition for W^* was thus rejected.

With the above considerations in mind, the definition proposed here will instead be

$$W^* = 4\,\mathrm{sgn}(\lambda_2)\sqrt{\frac{\lambda_1^2 + \lambda_2^2}{2}}, \qquad (36)$$

where $\mathrm{sgn}(x) = x/|x|$ is the sign function, the radical sign indicates the principal square root, and λ_1 and λ_2 are the first and second eigenvalues of $\mathbf{S}_{\mathrm{QG}}^2 + \mathbf{\Omega}_{\mathrm{QG}}^2$ (or both eigenvalues of $\mathbf{S}^2 + \mathbf{\Omega}^2$ for the 2D problem). The rationale for defining W^* in this way is as follows. Simple algebra can be used to show that $W^* = W$ when calculated for the 2D case using the eigenvalues of $\mathbf{S}^2 + \mathbf{\Omega}^2$, so that it is equivalent to the Okubo–Weiss parameter. In QG this definition of W^* includes terms involving $\mathbf{Q}$ and is equivalent to W in the limit where $\mathbf{u}_z = 0$, thereby reducing cleanly to the 2D case. In the QG case the magnitude of W^* remains the same even if λ_3 were substituted for λ_1 in (36), so it can be used to measure the strength of both vortex- and strain-dominated flows without biasing the magnitude one way or another. Finally, the sign function ensures that W^* retains the same sign as λ_2, and so retains the convenience of identifying vortices purely by its sign.[4]

In all, this exploration of the λ_2 criterion has led to several new parameters that can be used to partition QG flow structures based on their dynamics, magnitude, and geometry. A new parameter, W^*, has been introduced which reduces to W in 2D flows but improves upon the Okubo–Weiss parameter by accounting for the effects of baroclinicity. The vertical tilt of the flow structures diagnosed using W^* is indicated by the slope parameters, S_1 and S_3, which derive from the eigenvectors of $\mathbf{S}_{\mathrm{QG}}^2 + \mathbf{\Omega}_{\mathrm{QG}}^2$. The geometry of the eigenvectors has also been used to develop new parameters, Π_1 and Π_3, that describe the tilt of fronts and vortices, respectively. Each of these new

---

[4] Note that, by definition, W^* has the same sign as the standard Okubo–Weiss parameter and thus will identify the exact same vortical structures based on the criterion $W^* < 0$. However, most applications of the Okubo–Weiss parameter utilize some threshold value to distinguish eddies from other vortical structures, and similar thresholding will likely be required for W^*. Note that the optimal threshold for W will likely not be the same as for W^*, and both should be chosen on a case-by-case basis depending on the amount of noise in and resolution of the data.

parameters provides a way to describe ocean dynamics beyond the purely two-dimensional scope of the Okubo–Weiss parameter, which will be explored in the following section using high-resolution numerical model output.

4. Simulations

Both ocean observations and numerical simulations are appropriate for testing the new parameters developed in this paper. Given that it is standard practice to use the Okubo–Weiss parameter, a fundamentally 2D quantity, for diagnoses even in 3D flows, we are not necessarily limited to using strictly 2D or QG flows for these tests. Here we choose to test the new parameters using a high-resolution primitive equation numerical simulation, whose output depicts a highly turbulent eddy field and contains dense information about both the velocity and buoyancy fields. The simulation output thus allows the new parameters to be diagnosed for many different types of flow structures, just as they would be applied for real ocean flows.

The simulation examined here is the same as was used in Bachman and Klocker (2020), whose key features are summarized below. The MITgcm (Marshall et al. 1997) was used to perform a 5-yr experiment of the Kerguelen Plateau region at 1/120° resolution (nominally 650-m grid spacing in each direction), with a domain extending from 60° to 85°E in the zonal direction and from 50° to 38°S in the meridional direction. The vertical grid consisted of 150 layers of varying thickness, ranging from 10 m at the surface to 50 m at depth. Open boundary conditions were used to force the model at the lateral boundaries, where the velocity, temperature, and salinity fields were forced using daily output from a larger simulation of the Indian Ocean sector of the Southern Ocean (Klocker 2018). A 1/2°-wide sponge layer was used to relax the model to the boundary conditions, with a one-day relaxation time scale at the inner edge of the sponge and a 4-h time scale at the outer edge of the sponge. The wind and buoyancy forcing was derived from annually and zonally averaged output from the Southern Ocean State Estimate (Mazloff et al. 2010) and applied as meridionally varying but constant-in-time forcing over the model domain.

Instantaneous snapshots of the velocities and buoyancy field were written out every six hours during the final year of simulated time. Given the very tight horizontal grid spacing, each snapshot resolved a vigorous and fast-evolving eddy field at nearly submesoscale-resolving resolution. While larger flow structures such as mesoscale eddies would be expected to exhibit QG dynamics, the submesoscale structures in the model feature Rossby numbers that are too large and balanced Richardson numbers that are too small for QG scaling to be appropriate (Thomas et al. 2008). The small-scale dynamics in the simulation are thus admittedly outside both the 2D and QG regimes that underpin the theory here. However, W and the λ_2 criterion are intended to be applied to real ocean flows which do not fit neatly into either of these dynamical boxes either. The high-resolution simulation thus provides a realistic, rigorous, and challenging setting in which to test and compare the new parameters. Snapshots from day 100 and day 300 of the fifth year were arbitrarily chosen to demonstrate the new parameters developed in this paper. A region of particularly vigorous mesoscale turbulence stretching from 74° to 84°E and from 50° to 43°S was selected for visualization of these diagnostics, as it was large enough to permit several distinct vortical and frontal structures while being small enough to clearly view features at $\mathcal{O}(1)$ km scales. While these structures are clearly visible in both the maps of surface buoyancy (Fig. 2a) and vorticity (Fig. 2b), neither field clearly delineates what types of dynamics are dominant at a given point in space, justifying the need for more rigorous identification methods as are explored here.

The middle and bottom rows of Fig. 2 show visualizations of the Okubo–Weiss parameter (labeled with a reminder that it is equal to 4 times the middle eigenvalue of $\mathbf{S}_{\mathrm{QG}}^2 + \mathbf{\Omega}_{\mathrm{QG}}^2$; Fig. 2c), the new parameter W^* (Fig. 2d), and the first and third eigenvalues of $\mathbf{S}_{\mathrm{QG}}^2 + \mathbf{\Omega}_{\mathrm{QG}}^2$ (Figs. 2e,f). As demonstrated in numerous prior studies, the Okubo–Weiss parameter clearly singles out vortical structures as blue (negative) disk-shaped structures of various sizes that are interspersed throughout the domain. Many of the vortices are ringed by regions of positive W (red), which tend to occur in elongated, thin sets that are typical of strained density fronts. A key property to note is that these fronts, as visualized by W, tend to appear broken up into shorter segments reminiscent of dashed lines, rather than elongated, continuous streamers. This behavior is easily contrasted with the visualization of W^* (Fig. 2d), where the fronts are readily seen as continuous structures with very large magnitude. The subpanels above Figs. 2c and 2d show a magnified view of a region where these characteristics of W and W^* are especially apparent.

Here the reader is reminded that the sign of W^* and W *are the same at every point*, so the main visual difference between Figs. 2c and 2d is due to baroclinicity that is accounted for by the $|\mathbf{Q}|$ terms in W^*. Likewise, though all vortices in Fig. 2c still have negative values in Fig. 2d, the more baroclinic vortices stand out in Fig. 2d. Many of the vortices in Fig. 2d also appear as "doughnut" structures rather than disks because the baroclinicity is weakest at the vortex core. Last, note that the baroclinicity contributes significantly to the overall magnitude of the W^* diagnostic, and as such the color scale in Fig. 2d is an order of magnitude larger than that of Fig. 2c. Figures 2e and 2f also are shown at this enlarged color scale, and confirm that eigenvalues λ_1 and λ_3 are positive- and negative-definite, as stated earlier. Histograms comparing the magnitudes of W and W^* also demonstrate the relative significance of the $|\mathbf{Q}|$ terms (Fig. 3), such that the shapes of the respective histograms are very similar (both approximately lognormal) but the W^* histogram is shifted approximately an order of magnitude toward more extreme values.

The middle row of Fig. 2 suggests that an advantage of the new parameter W^* lies in its tendency to identify highly baroclinic frontal structures, which are not as clearly shown by W. This feature of W^* can be understood by examining the (inviscid) QG evolution equation for the buoyancy gradient magnitude,

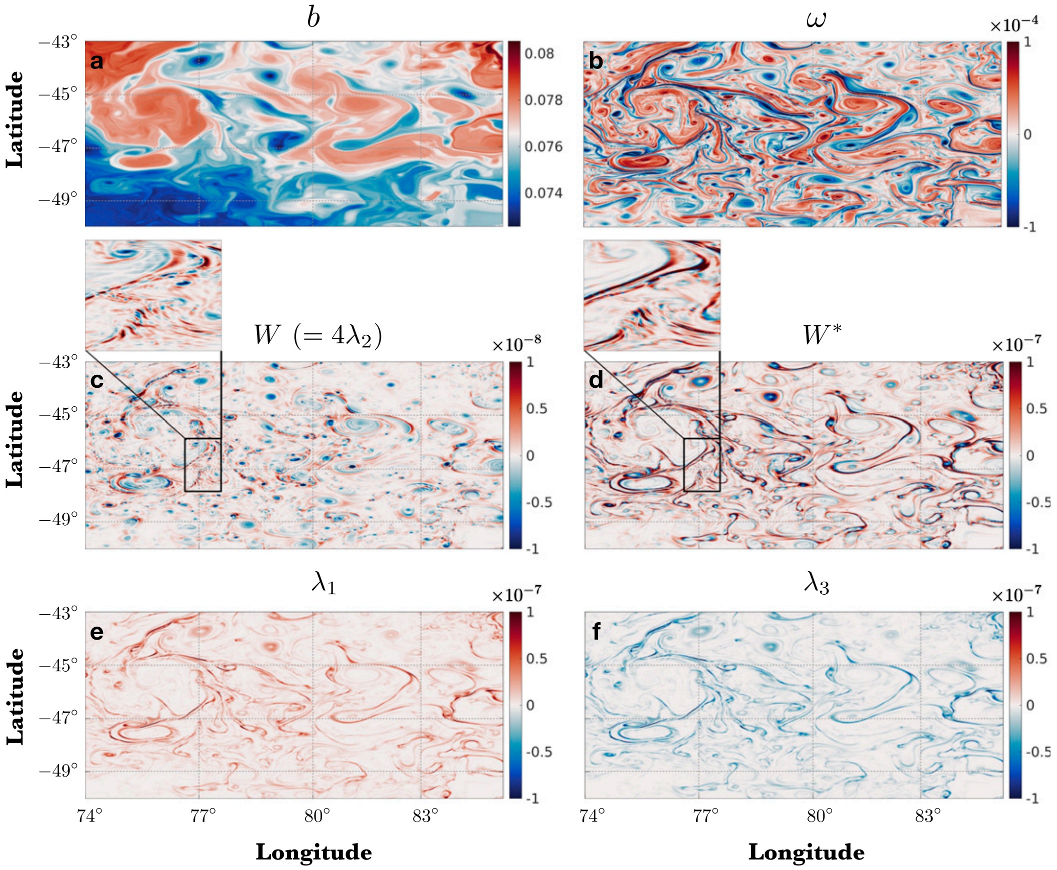

FIG. 2. Visualizations of (a) surface buoyancy, (b) relative vorticity, (c) W, (d) W^*, and the (e) first and (f) third eigenvalues of $\mathbf{S}_{\mathrm{QG}}^2 + \mathbf{\Omega}_{\mathrm{QG}}^2$, taken on year 5, day 100. Note the different color scale in (c) from (d)–(f).

$$\frac{D|\nabla_h b|}{Dt} = F - N^2\nabla_h w \cdot \frac{\nabla_h b}{|\nabla_h b|}, \qquad (37)$$

$$F = 2\mathbf{Q} \cdot \frac{\nabla_h b}{|\nabla_h b|}, \qquad (38)$$

where F is the frontogenesis function (Hoskins 1982). By (38) it is clear that the $\mathbf{Q}$ vector and F are closely related, such that one might expect a relationship $|\mathbf{Q}| \propto |F|$ to generally hold. Furthermore, by writing the definition of the λ_1 vector in the form $\mathbf{Q} = -\nabla_h \mathbf{u}^{\mathrm{T}} \cdot \nabla_h b$, one might also expect $|\mathbf{Q}| \propto |\nabla_h b|$. The dependence of W^* on the $|\mathbf{Q}|$ term in λ_1 would then suggest that the magnitude of W^* would be especially amplified where fronts are evolving rapidly and the buoyancy gradient is tight.

Figure 4 shows that these proposed relationships are supported well by the results from the numerical model. The first column shows intensity (scatter) plots of $|W|$ (top) and $|W^*|$ (bottom) against $|F|$ in logarithmic space. As in Fig. 3, these plots are produced using all surface points in the model subdomain, where lighter colors indicate a greater number of occurrences. The intensity plot for $|W|$ demonstrates only a weak trend with $|F|$, as indicated by the wide bullseye structure of the cloud of points. The Pearson's correlation coefficient between these two variables is 0.28. In contrast, the intensity plot for $|W^*|$ shows a strongly linear and positive trend with $|F|$, with a correlation coefficient of 0.88. Note that individual points in the intensity plot are restricted to lie above the line

$$\log_{10}|W^*| = \frac{1}{2}\log_{10}|F| - \frac{1}{2}\log_{10}4|f_0|, \qquad (39)$$

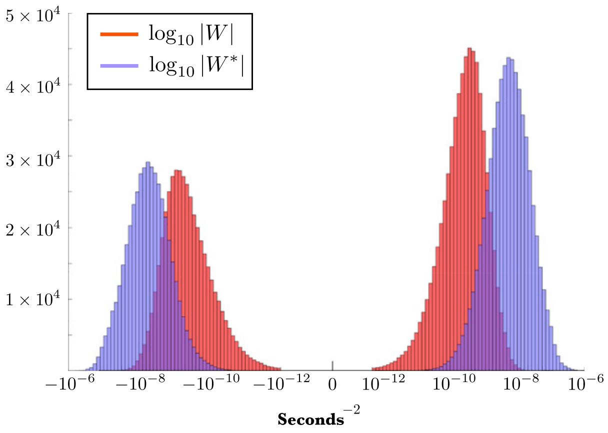

FIG. 3. Histograms of the base-10 logarithm of W and W^*, taken over all surface points in the model subdomain at year 5, day 100.

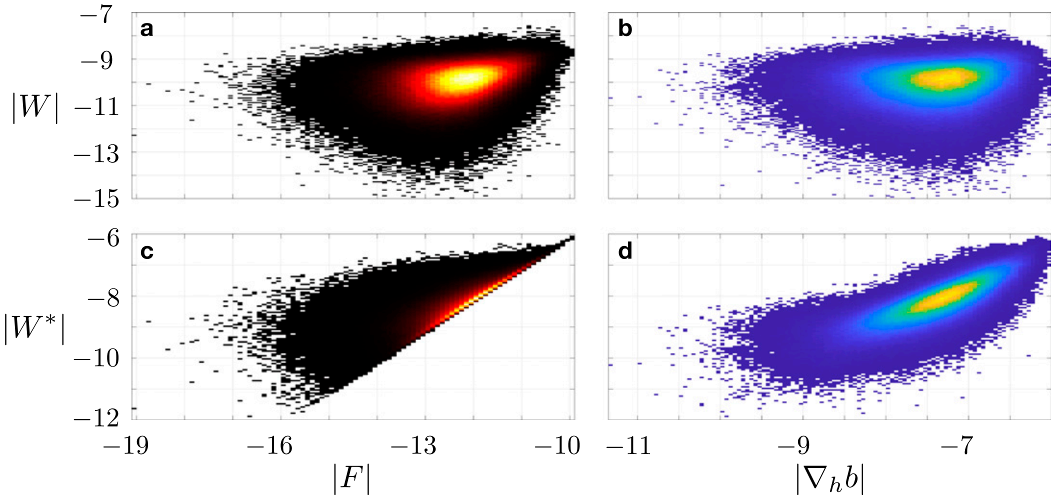

FIG. 4. Intensity plots showing the relationship between the magnitudes of F, $\nabla_h b$, W, and W^* in logarithmic space. Values for these plots are gathered from surface points on year 5, day 100.

which can be straightforwardly derived by using (36) and (38) to establish an inequality between $\log_{10}|W^*|$ and $\log_{10}|F|$. Intensity plots for $\log_{10}|\nabla_h b|$ (right column) show similar behavior; although no useful bounds can be derived in this case, the logarithm of $|W^*|$ exhibits a much clearer trend with $\log_{10}|\nabla_h b|$ (correlation coefficient 0.81) than does the logarithm of $|W|$ (0.13).

The close relationship between F, $|\nabla_h b|$, and W^* is also clearly visible in spatial maps of these variables (Fig. 5), particularly with regard to strong frontal structures. Each panel of this figure shows values measured on year 5, day 100, where the range of the color axes are chosen to highlight how the tightest fronts and filaments are easily seen in all three metrics and match quite well between them. A particularly interesting result emerges by considering weaker values of these variables as well, where forming histograms of their magnitudes in logarithmic space reveals that all three have approximately lognormal distributions (Fig. 6). For the sake of identifying fronts by employing a threshold value on W^*, this implies that a threshold based on standard deviations of $\log_{10}|W^*|$ would be likely to isolate the same strong features as would emerge by applying a threshold on the standard deviations of $\log_{10}|F|$ or $\log_{10}|\nabla_h b|$.

Figure 7 shows the result of applying such a threshold to each of these variables. The vast majority of the features shown here are strain-dominated fronts, since they tend to be associated with larger values of $|\mathbf{Q}|$ than do vortices. In these plots an overbar represents the mean and σ represents the standard deviation of each variable's magnitude in logarithmic space. Each panel shows the structures that are identified by taking only those points with magnitudes stronger than the mean plus half a standard deviation (first column), the mean plus one standard deviation (second column), and the mean plus 1.5 standard deviations (third column). Naturally, each column represents a progressively stronger filter moving from left to right across this figure (keeping approximately 31%, 16%, and 7% of points, respectively), which results in detecting fewer and thinner segments of these features. As seen previously in Figs. 6b–d, there is very close agreement between each variable in terms of which structures are detected, with differences generally pertaining to the precise size and shape of each feature. A noteworthy exception is highlighted in the green box in Fig. 7a, where a strongly vortical eddy (detected by all three metrics due to a strong temperature contrast between its fringe and its core) is detected quite clearly by the W^* metric but slightly less so for the other two. For the stronger filters in the right two columns, more of this eddy is able to pass through the filter on W^*, whereas it is effectively filtered out completely as measured by F and $\nabla_h b$. In practical terms these differences are unlikely to matter, since none of these variables are materially conserved and do not truly represent the stability of fluid trajectories in any case (e.g., Haller 2005); their similarity is presented here only to confirm the utility of W^* for detecting strongly baroclinic structures.

To emphasize the superior skill of W^* at identifying frontal structures, the bottom row of Fig. 7 shows the same standard deviation-based thresholds applied to $\log_{10}|W|$. In all three columns it is clear that W identifies an entirely different set of structures that are more circular in shape, which is indicative of its facility at identifying eddies in comparison to its identification of fronts (see also the discussion of Fig. 2).

Finally, Fig. 8 shows a map of the strain and vortex tilt as predicted by the new parameters, Π_1 and Π_3, respectively. The maps in Figs. 8b and 8d are filtered so that only regions where $W > 0$ and $W < 0$ are shown in color, respectively. Figures 8a and 8c show the frequency at which each value of Π_1 and Π_3 occurs in the map, where the vertical axis is in logarithmic scale. The convexity of the PDFs in Figs. 8a and 8c indicate that the distributions are not quite exponential, but are nonetheless dominated by values near -1 and 1, respectively. Likewise, Figs. 8b and 8d are dominated by darker shades, indicating values near $|1|$, except for some conspicuous regions of orange shading within certain vortices in Fig. 8d. As noted in section 3a, smaller values indicate where W is dominant over

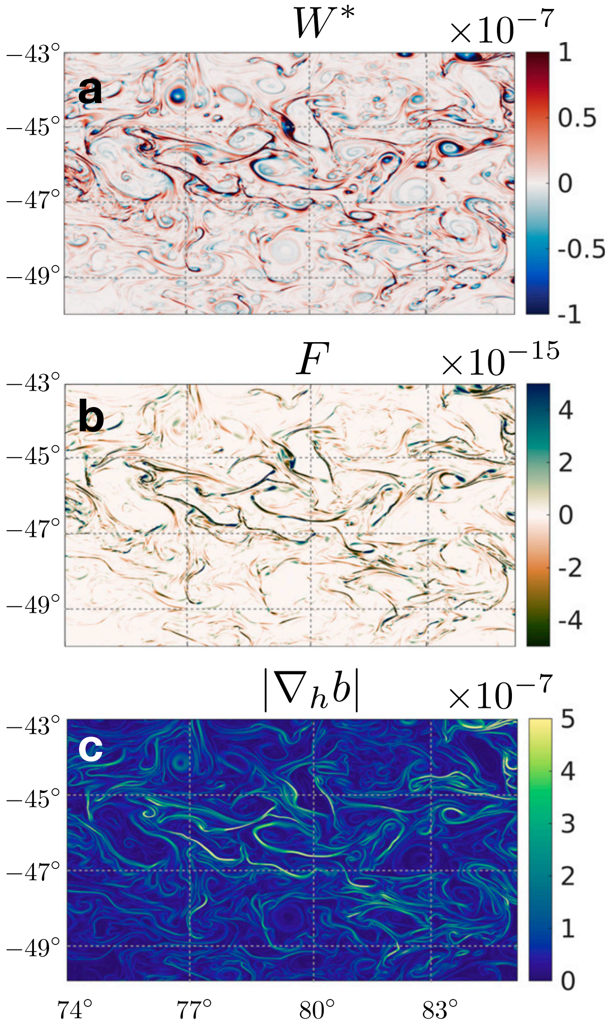

FIG. 5. Spatial maps of (a) W^*, (b) the frontogenesis function, and (c) the horizontal buoyancy gradient magnitude, highlighting their similarities for identifying strong fronts and filaments on year 5, day 100.

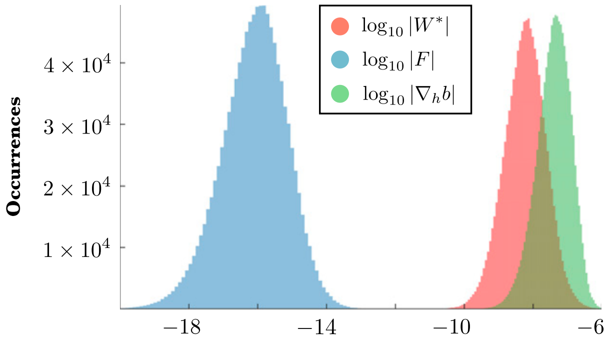

FIG. 6. Histograms of the magnitudes of F, $\nabla_h b$, and W^* in logarithmic space, on year 5, day 100. Note that all three histograms show approximately lognormal distributions.

the contribution of $|\mathbf{Q}|/f_0$, or where the baroclinicity is relatively weak. It is curious, though not necessarily noteworthy, that only a very small number of structures seem to bear this characteristic.

Several other diagnostics were compared to the spatial maps of Π_1 and Π_3 to try to discern whether there exist correlations with other features of the flow. Among these were mixed layer depth, ratio of shear production to buoyancy flux (essentially to determine whether energy conversion in these eddies was more associated with lateral or vertical shears), and vortex size, but no firm correlations were found with any of these features. It is possible that Π_1 and Π_3 may be relatable to other, more complicated questions about ocean eddies—how do these parameters evolve over the lifetime of an eddy, for example, or is there any connection with the amount or distance of water mass transport—that are beyond the scope and capability of this dataset. It is also possible that Π_1 and Π_3 are simply mathematical novelties, given that they essentially represent the degree of structural tilt despite that the 3D QG equations have no vortex tilting term. Their precise relationship with the curvature of the pressure field could also be investigated, though it would require a specially designed QG model to do so since the steepest slopes of |1| are not resolvable with the aspect ratio, $\Delta z/\Delta x = \mathscr{O}(10^{-3})$, of a typical eddy-resolving ocean model. For now these questions are posed here to motivate future investigation into this topic, and the results in Fig. 8 are shown for completeness and consistency with the theory from section 3a.

5. Discussion and conclusions

A new Eulerian vortex detection scheme has been developed that aims to differentiate vorticity-dominated and strain-dominated regions in realistic ocean flows. Like other, earlier methods that are popularly used for eddy detection in observational and computational oceanography, the scheme differentiates these regions based on the velocity gradients of the flow. The motivation for the new scheme is the ocean's quasi-two-dimensional behavior at large scales, which nonetheless features vertical shear and horizontal density gradients that are not accounted for by other methods that are based on the eigenvalues of the velocity gradient tensor. This issue stems from the fact that the nonzero eigenvalues of the 2D and QG velocity gradient tensors are identical, resulting in a mathematical degeneracy wherein the vertical shear is ignored. It is shown here, via pathological example, that the vertical shear can play a leading-order role in the evolution of tracer gradients in QG flow, thus necessitating a new scheme that accounts for the vertical dimension.

Under the QG approximation the vertical and horizontal dimensions are coupled through thermal wind balance. In principle this allows a scheme to be developed that is sensitive to dynamics in the vertical while still only measuring quantities in a horizontal plane, e.g., at the surface. In fact, since the QG tracer gradient problem is decoupled between the horizontal and vertical directions and the vertical shear only affects the vertical tracer gradient (e.g., Hua et al. 1998; Smith and Ferrari 2009), the information gained by measuring the vertical shear

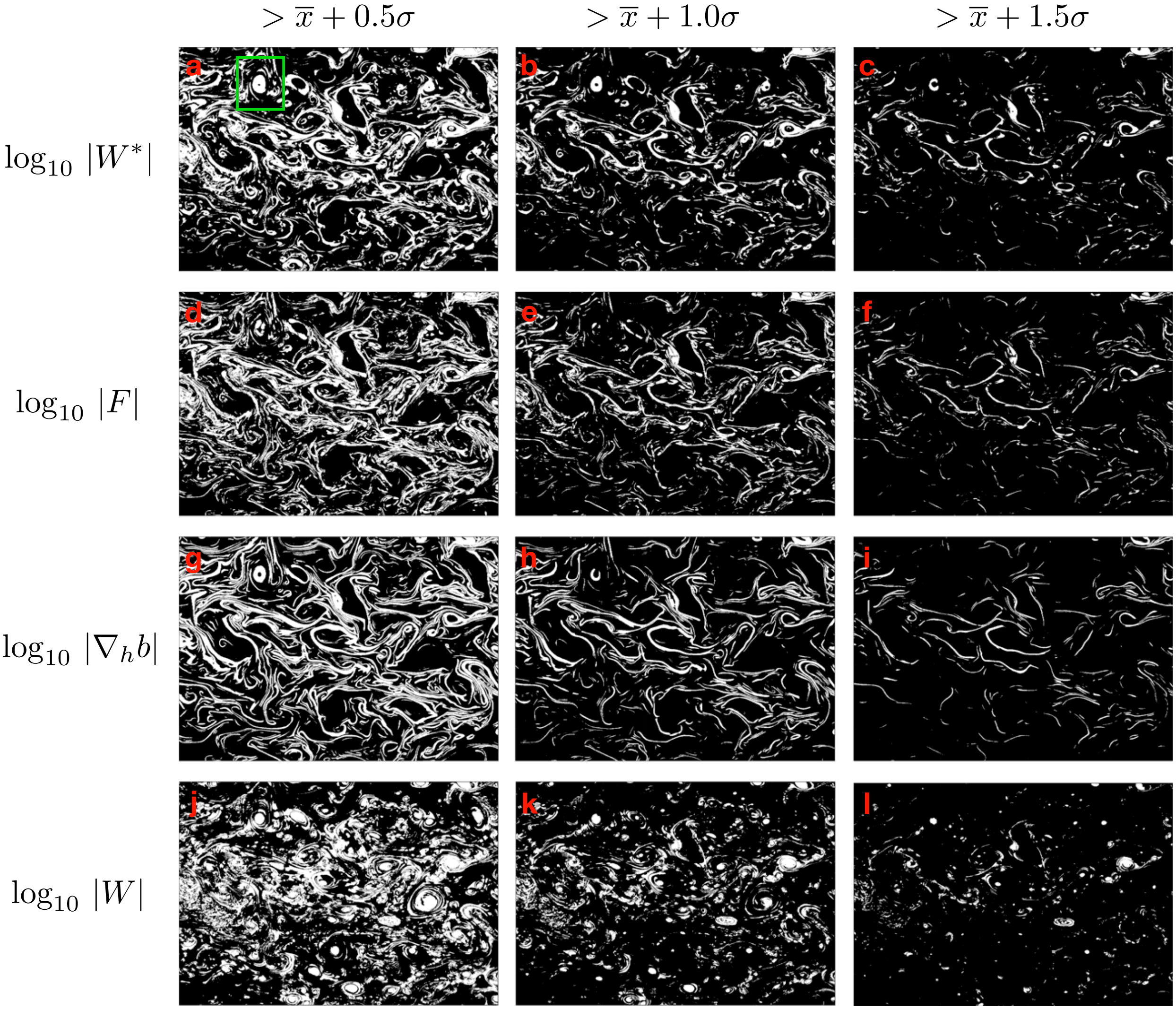

FIG. 7. Baroclinic structures detected by applying a threshold filter to the magnitudes of W^*, F, $\nabla_h b$, and W in logarithmic space. The lognormal probability distributions for each variable (Fig. 6) suggest that these thresholds can be defined using standard deviations. Regions in white indicate where the magnitude is greater than the mean plus (left) 0.5, (center) 1.0, and (right) 1.5 standard deviations. The green box identifies an exceptionally baroclinic eddy. Values for these plots are gathered from surface points on year 5, day 300.

(the horizontal buoyancy gradient) is *specific to* the tracer evolution in the vertical. It is thus natural that a scheme that includes the horizontal buoyancy gradient would be sensitive those features where vertical dynamics are known to be significant, i.e., fronts and filaments.

The scheme developed here is based on the QG version of the λ_2 criterion (Jeong and Hussain 1995), which decomposes the flow based on the eigenvalues of a different tensor of velocity gradients, $\mathbf{S}^2 + \mathbf{Q}^2$, and so avoids the mathematical degeneracy problem. This approach reduces neatly to the Okubo–Weiss parameter W for purely 2D flow, but in QG its eigenvalues include a combination of vorticity and straining in the horizontal plane as well as a baroclinic term involving the $\mathbf{Q}$ vector. Being a geometric object, the $\mathbf{S}^2 + \mathbf{Q}^2$ tensor is also examined in terms of its eigenvectors, and it is shown that their orientation is restricted to be predominantly horizontal under the QG approximation. Finally, a new parameter W^* is derived that is everywhere the same sign as W, and that smoothly transitions to it the limit of no vertical shear (i.e., purely 2D flow). It thus identifies the exact same vortices as does W, with the proviso that their distributions are different and thus filtering methods using thresholds (e.g., Elhmaïdi et al. 1993) may affect them differently. The new parameter is applied to a sample flow field taken from a high-resolution regional MITgcm simulation, and is shown to be superior to W for identifying strong fronts and filaments, whose dynamics are dominated by baroclinic effects associated with $\mathbf{Q}$. It is further shown that there is a very close association between W^*, fronts, and the frontogenesis function, such that W^* is equally useful for identifying strongly strained features as well as vortices. Because W^* is a direct extension of W, i.e., one can exactly recover W by omitting the horizontal buoyancy gradient term, one can use W^* to cleanly separate how the flow dynamics

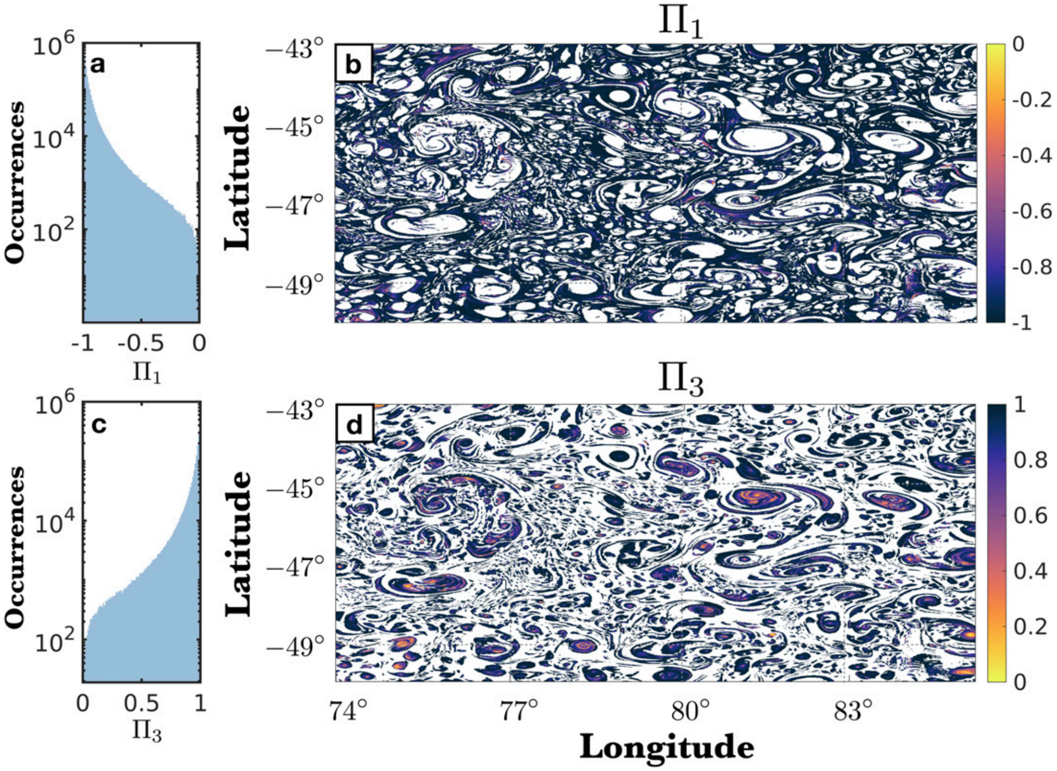

FIG. 8. (a) Number of occurrences for each value of Π_1 from (b) its spatial distribution throughout the model subdomain on year 5, day 100. (c),(d) Analogous results pertaining to Π_3.

are affecting horizontal gradients (W) versus vertical gradients ($W^* - W$).

Vortex detection parameters are employed both for the analysis of remote sensing data and numerical model output, typically for estimating tracer transport by coherent eddies. A main advantage of 2D parameters like W is that they are naturally applied to data observed at the sea surface, which are readily available and densely sampled compared to observations at depth. The new parameter W^* takes advantage of the predominantly geostrophic nature of large-scale flows that relates the vertical shear to horizontal density gradients via thermal wind balance, thus also being applicable to 2D (sea surface) flows despite including 3D dynamics. One of the primary advantages of W^* is that it gives a window into vertical gradient dynamics despite only requiring 2D data. Many tracers considered to be important by oceanographers are either primarily forced at the surface (heat, via surface heat fluxes) or tend to collect near the surface (buoyant pollutants like oil, or chlorophyll), which would naturally establish vertical gradients. The evolution of the vertical gradients implied by large W^* thus indicates important processes such as subduction or ventilation are occurring (i.e., the dynamics are stretching out or contracting the gradients, respectively), particularly at small-scale strain dominated regions as found by Balwada et al. (2021). Indeed, the new scheme has been shown to be superior at detecting precisely those features where subduction is known to strongly occur, such as fronts, filaments, and the fringes of coherent eddies (e.g., Stukel et al. 2017; Taylor et al. 2018; Freilich and Mahadevan 2020).

A subtle issue regarding how to apply W^* concerns the kind of datasets for which it is most suitable. Parameters such as W are generally used only for vortex detection, not the detection of fronts, and are thus advantaged by the large [$\mathcal{O}(10\text{–}100)$ km] size of ocean mesoscale eddies. Fronts and filaments are significantly smaller, often of $\mathcal{O}(1)$ km width (McWilliams 2019), and thus are not typically resolved by current observational platforms. For this reason W^* presently is most well suited for the analysis of very high-resolution model output which resolves both large vortices and the fronts in the interstices. Future, high-resolution observing missions (e.g., Fu et al. 2009; Kilic et al. 2018; Rodríguez-Fernández et al. 2019) promise to open up applications for W^* within the space of observational oceanography. It is also possible that innovative methods using high-resolution satellite imagery, which are already used for the detection of ocean fronts (e.g., Bouali et al. 2015), could be developed for more near-term use.

The ability of W^* to include baroclinicity in its measure of vortex strength is the primary way it is distinguished from W. Since by construction it has the same sign as W everywhere, it can essentially be considered a reweighted version of the Okubo–Weiss parameter that is particularly sensitive to nearly geostrophic, baroclinic features. This feature of W^* is precisely what enables it to perform so well at identifying fronts and filaments, and may be useful for differentiating eddies based on their geometry (Fig. 8). However, for eddy *detection* it has the same limitations as W, namely, that it can be prone to misidentifying vorticity-dominated filaments as eddies (Fig. 2d). It also has the tendency to visually identify vortices as doughnuts rather than disks, since at the center of a vortex the $|\mathbf{Q}|$ term reaches its minimum, which may require automated vortex identification methods to be adjusted. Related to this point, baroclinicity causes W^* to take on a far larger range of values than W, and one notable risk is that using a standard deviation-based threshold to distinguish eddies from the background flow may cause the scheme to miss the more weakly baroclinic vortices. For these reasons, users may find it more useful to simply use W for the vortex detection step, and then to employ W^* as an auxiliary means of analysis or for the particular application of filament identification.

Finally, it is important to note the relative merits of Eulerian vortex identification methods such as W^* versus those of Lagrangian methods (e.g., Beron-Vera et al. 2013; Froyland et al. 2015; Haller et al. 2016; Wang et al. 2016; Abernathey and Haller 2018). Several disadvantages of Eulerian methods are discussed by Haller (2015), most notably that they are not objective (i.e., the identified structures may differ depending on the rotation or translation of the reference frame) and are materially incoherent (subject to significant leakage through the identified boundaries of the structures). Eulerian methods thus tend to strongly overestimate the degree of material coherence of eddies, as well as the volume of fluid that remains trapped within the eddy core (Liu et al. 2019). For quantifying water mass transport by coherent eddies in large-scale or temporally filtered flows, Lagrangian methods are thus clearly superior. However, recent work by Sinha et al. (2019) demonstrated that Lagrangian methods are challenged at submesoscale- and internal gravity wave-resolving resolutions, where the appearance of intricate small-scale structures can obscure the large-scale transport barriers in the flow. They also found that high-frequency motions can lead to substantially higher leakage than would be detected if one instead used filtered velocities, meaning that Lagrangian methods might also overestimate material coherence when applied to observed (coarser-scale) velocity fields.

It is also important to note that the lifespan of an eddy does not necessarily coincide with the time that a bolus of water is trapped inside it. That is, eddies may persist even after leaking water, so Lagrangian methods may not be necessary for applications that do not require strict material coherence, such as tracking eddy lifetimes, propagation distance, or mechanisms of dissipation. Furthermore, Lagrangian methods are computationally very expensive, requiring high temporal resolution and millions of advected particles to realize their full potential. In comparison, Eulerian methods only require instantaneous snapshots of the flow field, and are cheap enough to be used over the entire globe for significant duration of time. They thus retain an important place in the study of ocean turbulence, and continue to be employed in the modern oceanographic literature (e.g., Faghmous et al. 2015; Cetina-Heredia et al. 2019). A novel parameter like W^* that is capable of simultaneously detecting both eddies and fronts may open up new frontiers in how Eulerian methods are used, and future work will continue to explore this possibility.

Acknowledgments. This material is based upon work supported by the National Center for Atmospheric Research (NCAR), which is a major facility sponsored by the National Science Foundation under Cooperative Agreement 1852977.

Data availability statement. The numerical ocean model is available at http://mitgcm.org/. Additional data related to this paper may be requested from the author.

REFERENCES

Abernathey, R., and G. Haller, 2018: Transport by Lagrangian vortices in the eastern Pacific. *J. Phys. Oceanogr.*, **48**, 667–685, https://doi.org/10.1175/JPO-D-17-0102.1.

Ashurst, W. T., A. Kerstein, R. Kerr, and C. Gibson, 1987: Alignment of vorticity and scalar gradient with strain rate in simulated Navier–Stokes turbulence. *Phys. Fluids*, **30**, 2343–2353, https://doi.org/10.1063/1.866513.

Bachman, S. D., and A. Klocker, 2020: Interaction of jets and submesoscale dynamics leads to rapid ocean ventilation. *J. Phys. Oceanogr.*, **50**, 2873–2883, https://doi.org/10.1175/JPO-D-20-0117.1.

Balmforth, N. J., W. R. Young, J. Fields, J.-L. Thiffeault, and C. Pasquero, 2000: Stirring and mixing: 1999 program of summer study in geophysical fluid dynamics. Tech. Rep. WHOI-2000-07, Woods Hole Oceanographic Institution, 302 pp., https://doi.org/10.1575/1912/94.

Balwada, D., Q. Xiao, S. Smith, R. Abernathey, and A. R. Gray, 2021: Vertical fluxes conditioned on vorticity and strain reveal submesoscale ventilation. *J. Phys. Oceanogr.*, **51**, 2883–2901, https://doi.org/10.1175/JPO-D-21-0016.1.

Basdevant, C., and T. Philipovitch, 1994: On the validity of the "Weiss criterion" in two-dimensional turbulence. *Physica D*, **73**, 17–30, https://doi.org/10.1016/0167-2789(94)90222-4.

Berdahl, C., and D. Thompson, 1993: Eduction of swirling structure using the velocity gradient tensor. *AIAA J.*, **31**, 97–103, https://doi.org/10.2514/3.11324.

Beron-Vera, F. J., Y. Wang, M. J. Olascoaga, G. J. Goni, and G. Haller, 2013: Objective detection of oceanic eddies and the Agulhas leakage. *J. Phys. Oceanogr.*, **43**, 1426–1438, https://doi.org/10.1175/JPO-D-12-0171.1.

Bouali, M., O. Sato, and P. Polito, 2015: An algorithm to improve the detection of ocean fronts from whiskbroom scanner images. *Remote Sens. Lett.*, **6**, 942–951, https://doi.org/10.1080/2150704X.2015.1093187.

Cetina-Heredia, P., M. Roughan, E. van Sebille, S. Keating, and G. B. Brassington, 2019: Retention and leakage of water by mesoscale eddies in the East Australian Current system. *J. Geophys. Res. Oceans*, **124**, 2485–2500, https://doi.org/10.1029/2018JC014482.

Chakraborty, P., S. Balachandar, and R. J. Adrian, 2005: On the relationships between local vortex identification schemes. *J. Fluid Mech.*, **535**, 189–214, https://doi.org/10.1017/S0022112005004726.

Chelton, D. B., M. G. Schlax, R. M. Samelson, and R. A. de Szoeke, 2007: Global observations of large oceanic eddies. *Geophys. Res. Lett.*, **34**, L15606, https://doi.org/10.1029/2007GL030812.

——, ——, and ——, 2011: Global observations of nonlinear mesoscale eddies. *Prog. Oceanogr.*, **91**, 167–216, https://doi.org/10.1016/j.pocean.2011.01.002.

Chen, R., G. R. Flierl, and C. Wunsch, 2014: A description of local and nonlocal eddy–mean flow interaction in a global eddy-permitting state estimate. *J. Phys. Oceanogr.*, **44**, 2336–2352, https://doi.org/10.1175/JPO-D-14-0009.1.

Chen, S., R. E. Ecke, G. L. Eyink, X. Wang, and Z. Xiao, 2003: Physical mechanism of the two-dimensional enstrophy cascade. *Phys. Rev. Lett.*, **91**, 214501, https://doi.org/10.1103/physrevlett.91.214501.

Chevillard, L., C. Meneveau, L. Biferale, and F. Toschi, 2008: Modeling the pressure Hessian and viscous Laplacian in turbulence: Comparisons with direct numerical simulation and implications on velocity gradient dynamics. *Phys. Fluids*, **20**, 101504, https://doi.org/10.1063/1.3005832.

Chong, M. S., A. E. Perry, and B. J. Cantwell, 1990: A general classification of three-dimensional flow fields. *Phys. Fluids A*, **2**, 765–777, https://doi.org/10.1063/1.857730.

Donlon, C. J., M. Martin, J. Stark, J. Roberts-Jones, E. Fiedler, and W. Wimmer, 2012: The operational sea surface temperature and sea ice analysis (OSTIA) system. *Remote Sens. Environ.*, **116**, 140–158, https://doi.org/10.1016/j.rse.2010.10.017.

d'Ovidio, F., J. Isern-Fontanet, C. López, E. Hernández-García, and E. García-Ladona, 2009: Comparison between Eulerian diagnostics and finite-size Lyapunov exponents computed from altimetry in the Algerian basin. *Deep-Sea Res. I*, **56**, 15–31, https://doi.org/10.1016/j.dsr.2008.07.014.

Dritschel, D., P. Haynes, M. Juckes, and T. Shepherd, 1991: The stability of a two-dimensional vorticity filament under uniform strain. *J. Fluid Mech.*, **230**, 647–665, https://doi.org/10.1017/S0022112091000915.

Droghei, R., B. Buongiorno Nardelli, and R. Santoleri, 2018: A new global sea surface salinity and density dataset from multivariate observations (1993–2016). *Front. Mar. Sci.*, **5**, 84, https://doi.org/10.3389/fmars.2018.00084.

Elhmaïdi, D., A. Provenzale, and A. Babiano, 1993: Elementary topology of two-dimensional turbulence from a Lagrangian viewpoint and single-particle dispersion. *J. Fluid Mech.*, **257**, 533–558, https://doi.org/10.1017/S0022112093003192.

Faghmous, J. H., I. Frenger, Y. Yao, R. Warmka, A. Lindell, and V. Kumar, 2015: A daily global mesoscale ocean eddy dataset from satellite altimetry. *Sci. Data*, **2**, 150028, https://doi.org/10.1038/sdata.2015.28.

Ferrari, R., and C. Wunsch, 2009: Ocean circulation kinetic energy: Reservoirs, sources, and sinks. *Annu. Rev. Fluid Mech.*, **41**, 253–282, https://doi.org/10.1146/annurev.fluid.40.111406.102139.

——, and ——, 2010: The distribution of eddy kinetic and potential energies in the global ocean. *Tellus*, **62A**, 92–108, https://doi.org/10.1111/j.1600-0870.2009.00432.x.

Freilich, M., and A. Mahadevan, 2020: Coherent pathways for subduction from the surface mixed layer at ocean fronts. *J. Geophys. Res. Oceans*, **126**, e2020JC017042, https://doi.org/10.1029/2020JC017042.

Froyland, G., C. Horenkamp, V. Rossi, and E. Van Sebille, 2015: Studying an Agulhas ring's long-term pathway and decay with finite-time coherent sets. *Chaos*, **25**, 083119, https://doi.org/10.1063/1.4927830.

Fu, L.-L., D. Alsdorf, E. Rodriguez, R. Morrow, N. Mognard, J. Lambin, P. Vaze, and T. Lafon, 2009: The SWOT (Surface Water and Ocean Topography) mission: Spaceborne radar interferometry for oceanographic and hydrological applications. *Proceedings of OceanObs'09: Sustained Ocean Observations and Information for Society*, Vol. 2, J. Hall, D. E. Harrison, and D. Stammer, Eds., ESA Publication WPP-306, https://doi.org 10.5270/OceanObs09.cwp.33.

Galanti, B., J. Gibbon, and M. Heritage, 1997: Vorticity alignment results for the three-dimensional Euler and Navier-Stokes equations. *Nonlinearity*, **10**, 1675–1694, https://doi.org/10.1088/0951-7715/10/6/013.

Haller, G., 2005: An objective definition of a vortex. *J. Fluid Mech.*, **525**, 1–26, https://doi.org/10.1017/S0022112004002526.

——, 2015: Lagrangian coherent structures. *Annu. Rev. Fluid Mech.*, **47**, 137–162, https://doi.org/10.1146/annurev-fluid-010313-141322.

——, and G. Yuan, 2000: Lagrangian coherent structures and mixing in two-dimensional turbulence. *Physica D*, **147**, 352–370, https://doi.org/10.1016/S0167-2789(00)00142-1.

——, A. Hadjighasem, M. Farazmand, and F. Huhn, 2016: Defining coherent vortices objectively from the vorticity. *J. Fluid Mech.*, **795**, 136–173, https://doi.org/10.1017/jfm.2016.151.

Henson, S. A., and A. C. Thomas, 2008: A census of oceanic anticyclonic eddies in the Gulf of Alaska. *Deep-Sea Res. I*, **55**, 163–176, https://doi.org/10.1016/j.dsr.2007.11.005.

Herring, J. R., 1980: Statistical theory of quasi-geostrophic turbulence. *J. Atmos. Sci.*, **37**, 969–977, https://doi.org/10.1175/1520-0469(1980)037<0969:RDOWTS>2.0.CO;2.

Hoskins, B. J., 1982: The mathematical theory of frontogenesis. *Annu. Rev. Fluid Mech.*, **14**, 131–151, https://doi.org/10.1146/annurev.fl.14.010182.001023.

——, I. Draghici, and H. Davies, 1978: A new look at the ω-equation. *Quart. J. Roy. Meteor. Soc.*, **104**, 31–38, https://doi.org/10.1002/qj.49710443903.

Hua, B. L., and D. B. Haidvogel, 1986: Numerical simulations of the vertical structure of quasi-geostrophic turbulence. *J. Atmos. Sci.*, **43**, 2923–2936, https://doi.org/10.1175/1520-0469(1986)043<2923:NSOTVS>2.0.CO;2.

——, and P. Klein, 1998: An exact criterion for the stirring properties of nearly two-dimensional turbulence. *Physica D*, **113**, 98–110, https://doi.org/10.1016/S0167-2789(97)00143-7.

——, J. C. McWilliams, and P. Klein, 1998: Lagrangian accelerations in geostrophic turbulence. *J. Fluid Mech.*, **366**, 87–108, https://doi.org/10.1017/S0022112098001001.

Hunt, J. C., A. A. Wray, and P. Moin, 1988: Eddies, streams, and convergence zones in turbulent flows. *Studying Turbulence Using Numerical Simulation Databases – II: Proceedings of the Summer Program 1988*, Rep. CTR-S88, Center for Turbulence Researce, NASA, 193–208, http://web.stanford.edu/group/ctr/Summer/SP1988/19_HUNT.pdf.

Isern-Fontanet, J., E. García-Ladona, and J. Font, 2003: Identification of marine eddies from altimetric maps. *J. Atmos. Oceanic Technol.*, **20**, 772–778, https://doi.org/10.1175/1520-0426(2003)20<772:IOMEFA>2.0.CO;2.

——, J. Font, E. García-Ladona, M. Emelianov, C. Millot, and I. Taupier-Letage, 2004: Spatial structure of anticyclonic eddies in the Algerian basin (Mediterranean Sea) analyzed using the Okubo–Weiss parameter. *Deep-Sea Res. II*, **51**, 3009–3028, https://doi.org/10.1016/j.dsr2.2004.09.013.

——, E. Olmedo, A. Turiel, J. Ballabrera-Poy, and E. García-Ladona, 2016: Retrieval of eddy dynamics from SMOS sea surface salinity measurements in the Algerian Basin (Mediterranean Sea). *Geophys. Res. Lett.*, **43**, 6427–6434, https://doi.org/10.1002/2016GL069595.

Jeong, J., and F. Hussain, 1995: On the identification of a vortex. *J. Fluid Mech.*, **285**, 69–94, https://doi.org/10.1017/S0022112095000462.

Kevlahan, N.-R., and M. Farge, 1997: Vorticity filaments in two-dimensional turbulence: Creation, stability and effect. *J. Fluid Mech.*, **346**, 49–76, https://doi.org/10.1017/S0022112097006113.

Kilic, L., and Coauthors, 2018: Expected performances of the Copernicus Imaging Microwave Radiometer (CIMR) for an all-weather and high spatial resolution estimation of ocean and sea ice parameters. *J. Geophys. Res. Oceans*, **123**, 7564–7580, https://doi.org/10.1029/2018JC014408.

Klein, P., and G. Lapeyre, 2009: The oceanic vertical pump induced by mesoscale and submesoscale turbulence. *Annu. Rev. Mar. Sci.*, **1**, 351–375, https://doi.org/10.1146/annurev.marine.010908.163704.

——, B. L. Hua, and G. Lapeyre, 2000: Alignment of tracer gradient vectors in 2D turbulence. *Physica D*, **146**, 246–260, https://doi.org/10.1016/S0167-2789(00)00119-6.

Klocker, A., 2018: Opening the window to the Southern Ocean: The role of jet dynamics. *Sci. Adv.*, **4**, eaao4719, https://doi.org/10.1126/sciadv.aao4719.

Lapeyre, G., P. Klein, and B. Hua, 1999: Does the tracer gradient vector align with the strain eigenvectors in 2D turbulence? *Phys. Fluids*, **11**, 3729–3737, https://doi.org/10.1063/1.870234.

Lévy, M., R. Ferrari, P. J. Franks, A. P. Martin, and P. Rivière, 2012: Bringing physics to life at the submesoscale. *Geophys. Res. Lett.*, **39**, L14602, https://doi.org/10.1029/2012GL052756.

Liu, T., R. Abernathey, A. Sinha, and D. Chen, 2019: Quantifying Eulerian eddy leakiness in an idealized model. *J. Geophys. Res. Oceans*, **124**, 8869–8886, https://doi.org/10.1029/2019JC015576.

Madrid, J. J., and A. M. Mancho, 2009: Distinguished trajectories in time dependent vector fields. *Chaos*, **19**, 013111, https://doi.org/10.1063/1.3056050.

Mahadevan, A., and A. Tandon, 2006: An analysis of mechanisms for submesoscale vertical motion at ocean fronts. *Ocean Modell.*, **14**, 241–256, https://doi.org/10.1016/j.ocemod.2006.05.006.

Mancho, A. M., S. Wiggins, J. Curbelo, and C. Mendoza, 2013: Lagrangian descriptors: A method for revealing phase space structures of general time dependent dynamical systems. *Commun. Nonlinear Sci. Numer. Simul.*, **18**, 3530–3557, https://doi.org/10.1016/j.cnsns.2013.05.002.

Mariotti, A., B. Legras, and D. G. Dritschel, 1994: Vortex stripping and the erosion of coherent structures in two-dimensional flows. *Phys. Fluids*, **6**, 3954–3962, https://doi.org/10.1063/1.868385.

Marshall, J., A. Adcroft, C. Hill, L. Perelman, and C. Heisey, 1997: A finite-volume, incompressible Navier–Stokes model for studies of the ocean on parallel computers. *J. Geophys. Res.*, **102**, 5753–5766, https://doi.org/10.1029/96JC02775.

Mazloff, M. R., P. Heimbach, and C. Wunsch, 2010: An eddy-permitting southern ocean state estimate. *J. Phys. Oceanogr.*, **40**, 880–899, https://doi.org/10.1175/2009JPO4236.1.

McWilliams, J. C., 1984: The emergence of isolated, coherent vortices in turbulent flow. *AIP Conf. Proc.*, **106**, 205–221, https://doi.org/10.1063/1.34273.

——, 1989: Statistical properties of decaying geostrophic turbulence. *J. Fluid Mech.*, **198**, 199–230, https://doi.org/10.1017/S0022112089000108.

——, 2019: A survey of submesoscale currents. *Geosci. Lett.*, **6**, 3, https://doi.org/10.1186/s40562-019-0133-3.

Melander, M., J. McWilliams, and N. Zabusky, 1987: Axisymmetrization and vorticity-gradient intensification of an isolated two-dimensional vortex through filamentation. *J. Fluid Mech.*, **178**, 137–159, https://doi.org/10.1017/S0022112087001150.

Melnichenko, O., A. Amores, N. Maximenko, P. Hacker, and J. Potemra, 2017: Signature of mesoscale eddies in satellite sea surface salinity data. *J. Geophys. Res. Oceans*, **122**, 1416–1424, https://doi.org/10.1002/2016JC012420.

Morrow, R., F. Birol, D. Griffin, and J. Sudre, 2004: Divergent pathways of cyclonic and anti-cyclonic ocean eddies. *Geophys. Res. Lett.*, **31**, L24311, https://doi.org/10.1029/2004GL020974.

Nencioli, F., C. Dong, T. Dickey, L. Washburn, and J. C. McWilliams, 2010: A vector geometry–based eddy detection algorithm and its application to a high-resolution numerical model product and high-frequency radar surface velocities in the Southern California Bight. *J. Atmos. Oceanic Technol.*, **27**, 564–579, https://doi.org/10.1175/2009JTECHO725.1.

Ohkitani, K., and S. Kishiba, 1995: Nonlocal nature of vortex stretching in an inviscid fluid. *Phys. Fluids*, **7**, 411–421, https://doi.org/10.1063/1.868638.

Okubo, A., 1970: Horizontal dispersion of floatable particles in the vicinity of velocity singularities such as convergences. *Deep Sea Res. Oceanogr. Abstr.*, **17**, 445–454, https://doi.org/10.1016/0011-7471(70)90059-8.

Pedergnana, T., D. Oettinger, G. P. Langlois, and G. Haller, 2020: Explicit unsteady Navier–Stokes solutions and their analysis via local vortex criteria. *Phys. Fluids*, **32**, 046603, https://doi.org/10.1063/5.0003245.

Peng, B., 2007: The determinant: A means to calculate volume. *Recall*, **21**, a22, http://math.uchicago.edu/~may/VIGRE/VIGRE2007/REUPapers/INCOMING/voldets-2.pdf.

Petersen, M. R., K. Julien, and J. B. Weiss, 2006: Vortex cores, strain cells, and filaments in quasigeostrophic turbulence. *Phys. Fluids*, **18**, 026601, https://doi.org/10.1063/1.2166452.

——, S. J. Williams, M. E. Maltrud, M. W. Hecht, and B. Hamann, 2013: A three-dimensional eddy census of a high-resolution global ocean simulation. *J. Geophys. Res. Oceans*, **118**, 1759–1774, https://doi.org/10.1002/jgrc.20155.

Pierrehumbert, R. T., and H. Yang, 1993: Global chaotic mixing on isentropic surfaces. *J. Atmos. Sci.*, **50**, 2462–2480, https://doi.org/10.1175/1520-0469(1993)050<2462:GCMOIS>2.0.CO;2.

Poje, A. C., A. C. Haza, T. M. Özgökmen, M. G. Magaldi, and Z. D. Garraffo, 2010: Resolution dependent relative dispersion statistics in a hierarchy of ocean models. *Ocean Modell.*, **31**, 36–50, https://doi.org/10.1016/j.ocemod.2009.09.002.

Protas, B., A. Babiano, and N.-R. Kevlahan, 1999: On geometrical alignment properties of two-dimensional forced turbulence. *Physica D*, **128**, 169–179, https://doi.org/10.1016/S0167-2789(98)00301-7.

Reul, N., and Coauthors, 2014: Sea surface salinity observations from space with the SMOS satellite: A new means to monitor the marine branch of the water cycle. *Surv. Geophys.*, **35**, 681–722, https://doi.org/10.1007/s10712-013-9244-0.

——, and Coauthors, 2020: Sea surface salinity estimates from spaceborne L-band radiometers: An overview of the first decade of observation (2010–2019). *Remote Sens. Environ.*, **242**, 111769, https://doi.org/10.1016/j.rse.2020.111769.

Rodríguez-Fernández, N. J., and Coauthors, 2019: SMOS-HR: A high resolution L-band passive radiometer for Earth science and applications. *IGARSS 2019: 2019 IEEE Int. Geoscience and Remote Sensing Symp.*, Yokohama, Japan, IEEE, 8392–8395, https://doi.org/10.1109/IGARSS.2019.8897815.

Sadarjoen, I. A., and F. H. Post, 2000: Detection, quantification, and tracking of vortices using streamline geometry. *Comput. Graph.*, **24**, 333–341, https://doi.org/10.1016/S0097-8493(00)00029-7.

Serra, M., and G. Haller, 2016: Objective Eulerian coherent structures. *Chaos*, **26**, 053110, https://doi.org/10.1063/1.4951720.

Sinha, A., D. Balwada, N. Tarshish, and R. Abernathey, 2019: Modulation of lateral transport by submesoscale flows and inertia-gravity waves. *J. Adv. Model. Earth Syst.*, **11**, 1039–1065, https://doi.org/10.1029/2018MS001508.

Smith, K. S., and R. Ferrari, 2009: The production and dissipation of compensated thermohaline variance by mesoscale stirring. *J. Phys. Oceanogr.*, **39**, 2477–2501, https://doi.org/10.1175/2009JPO4103.1.

Souza, J. M. A. C., C. de Boyer Montegut, and P.-Y. Le Traon, 2011: Comparison between three implementations of automatic identification algorithms for the quantification and characterization of mesoscale eddies in the South Atlantic Ocean. *Ocean Sci.*, **7**, 317–334, https://doi.org/10.5194/os-7-317-2011.

Storch, J.-S., C. Eden, I. Fast, H. Haak, D. Hernández-Deckers, E. Maier-Reimer, J. Marotzke, and D. Stammer, 2012: An estimate of the Lorenz energy cycle for the world ocean based on the STORM/NCEP simulation. *J. Phys. Oceanogr.*, **42**, 2185–2205, https://doi.org/10.1175/JPO-D-12-079.1.

Straub, D. N., 2003: Instability of 2D flows to hydrostatic 3D perturbations. *J. Atmos. Sci.*, **60**, 79–102, https://doi.org/10.1175/1520-0469(2003)060<0079:IOFTHP>2.0.CO;2.

Stukel, M. R., and Coauthors, 2017: Mesoscale ocean fronts enhance carbon export due to gravitational sinking and subduction. *Proc. Natl. Acad. Sci. USA*, **114**, 1252–1257, https://doi.org/10.1073/pnas.1609435114.

Taburet, G., A. Sanchez-Roman, M. Ballarotta, M.-I. Pujol, J.-F. Legeais, F. Fournier, Y. Faugere, and G. Dibarboure, 2019: DUACS DT2018: 25 years of reprocessed sea level altimetry products. *Ocean Sci.*, **15**, 1207–1224, https://doi.org/10.5194/os-15-1207-2019.

Tarshish, N., R. Abernathey, C. Zhang, C. O. Dufour, I. Frenger, and S. M. Griffies, 2018: Identifying Lagrangian coherent vortices in a mesoscale ocean model. *Ocean Modell.*, **130**, 15–28, https://doi.org/10.1016/j.ocemod.2018.07.001.

Taylor, J. R., S. Bachman, M. Stamper, P. Hosegood, K. Adams, J.-B. Sallee, and R. Torres, 2018: Submesoscale Rossby waves on the Antarctic circumpolar current. *Sci. Adv.*, **4**, eaao2824, https://doi.org/10.1126/sciadv.aao2824.

Thomas, L. N., A. Tandon, and A. Mahadevan, 2008: Submesoscale processes and dynamics. Ocean Modeling in an Eddying Regime, Geophys. Monogr., Vol. 177, Amer. Geophys. Union, 17–38, https://doi.org/10.1029/177GM04.

Umbert, M., S. Guimbard, G. Lagerloef, L. Thompson, M. Portabella, J. Ballabrera-Poy, and A. Turiel, 2015: Detecting the surface salinity signature of Gulf Stream cold-core rings in Aquarius synergistic products. *J. Geophys. Res. Oceans*, **120**, 859–874, https://doi.org/10.1002/2014JC010466.

Vinogradova, N., and Coauthors, 2019: Satellite salinity observing system: Recent discoveries and the way forward. *Front. Mar. Sci.*, **6**, 243, https://doi.org/10.3389/fmars.2019.00243.

Von Hardenberg, J., J. McWilliams, A. Provenzale, A. Shchepetkin, and J. Weiss, 2000: Vortex merging in quasi-geostrophic flows. *J. Fluid Mech.*, **412**, 331–353, https://doi.org/10.1017/S0022112000008442.

Wang, Y., F. J. Beron-Vera, and M. J. Olascoaga, 2016: The life cycle of a coherent Lagrangian Agulhas ring. *J. Geophys. Res. Oceans*, **121**, 3944–3954, https://doi.org/10.1002/2015JC011620.

Weiss, J., 1991: The dynamics of enstrophy transfer in two-dimensional hydrodynamics. *Physica D*, **48**, 273–294, https://doi.org/10.1016/0167-2789(91)90088-Q.

Williams, S., M. Hecht, M. Petersen, R. Strelitz, M. Maltrud, J. Ahrens, M. Hlawitschka, and B. Hamann, 2011: Visualization and analysis of eddies in a global ocean simulation. *Comput. Graphics Forum*, **30**, 991–1000, https://doi.org/10.1111/j.1467-8659.2011.01948.x.

Zhou, J., R. J. Adrian, S. Balachandar, and T. Kendall, 1999: Mechanisms for generating coherent packets of hairpin vortices in channel flow. *J. Fluid Mech.*, **387**, 353–396, https://doi.org/10.1017/S002211209900467X.

Zlotnicki, V., Z. Qu, and J. Willis, 2019: MEaSUREs gridded sea surface height anomalies version 1812. PODAAC, accessed 29 March 2021, https://doi.org/10.5067/SLREF-CDRV2.